David Taylor Research Center

Bethesda. MD 20084–5000

Two Counter-Rotating Vortices Approaching a Free Surface in a Viscous Fluid

by

Samuel Ohring

Hans J. Lugt

DTIC
ELECTE
JUL 2 5 1989
S
B
D

MAJOR DTRC TECHNICAL COMPONENTS

CODE 011 DIRECTOR OF TECHNOLOGY, PLANS AND ASSESSMENT

12 SHIP SYSTEMS INTEGRATION DEPARTMENT

14 SHIP ELECTROMAGNETIC SIGNATURES DEPARTMENT

15 SHIP HYDROMECHANICS DEPARTMENT

16 AVIATION DEPARTMENT

17 SHIP STRUCTURES AND PROTECTION DEPARTMENT

18 COMPUTATION, MATHEMATICS & LOGISTICS DEPARTMENT

19 SHIP ACOUSTICS DEPARTMENT

27 PROPULSION AND AUXILIARY SYSTEMS DEPARTMENT

28 SHIP MATERIALS ENGINEERING DEPARTMENT

DTRC ISSUES THREE TYPES OF REPORTS:

1. **DTRC reports, a formal series,** contain information of permanent technical value. They carry a consecutive numerical identification regardless of their classification or the originating department.

2. **Departmental reports, a semiformal series,** contain information of a preliminary, temporary, or proprietary nature or of limited interest or significance. They carry a departmental alphanumerical identification.

3. **Technical memoranda, an informal series,** contain technical documentation of limited use and interest. They are primarily working papers intended for internal use. They carry an identifying number which indicates their type and the numerical code of the originating department. Any distribution outside DTRC must be approved by the head of the originating department on a case-by-case basis.

SECURITY CLASSIFICATION OF THIS PAGE

REPORT DOCUMENTATION PAGE

Form Approved
OMB No 0704-0188

1a REPORT SECURITY CLASSIFICATION	1b RESTRICTIVE MARKINGS
UNCLASSIFIED	

2a SECURITY CLASSIFICATION AUTHORITY	3 DISTRIBUTION/AVAILABILITY OF REPORT
	Approved for public release;
2b DECLASSIFICATION/DOWNGRADING SCHEDULE	distribution is unlimited.

4 PERFORMING ORGANIZATION REPORT NUMBER(S)	5 MONITORING ORGANIZATION REPORT NUMBER(S)
DTRC-89/013	

6a NAME OF PERFORMING ORGANIZATION	6b OFFICE SYMBOL (If applicable)	7a NAME OF MONITORING ORGANIZATION
David Taylor Research Center	Code 1843	

6c ADDRESS (City, State, and ZIP Code)	7b ADDRESS (City, State, and ZIP Code)
Bethesda, Maryland 20084-5000	

8a NAME OF FUNDING/SPONSORING ORGANIZATION	8b OFFICE SYMBOL (If applicable)	9 PROCUREMENT INSTRUMENT IDENTIFICATION NUMBER
Office of Naval Research		

8c. ADDRESS (City, State, and ZIP Code)	10 SOURCE OF FUNDING NUMBERS			
	PROGRAM ELEMENT NO	PROJECT NO	TASK NO	WORK UNIT ACCESSION NO
Arlington, Virginia 22217	61153N	RR0140302		DN 509003

11 TITLE (Include Security Classification)

TWO COUNTER-ROTATING VORTICES APPROACHING A FREE SURFACE IN A VISCOUS FLUID

12 PERSONAL AUTHOR(S)
Ohring, Samuel and Lugt, Hans J.

13a TYPE OF REPORT	13b TIME COVERED	14 DATE OF REPORT (Year, Month, Day)	15 PAGE COUNT
Final	FROM ___ TO ___	1989 June	64

16 SUPPLEMENTARY NOTATION

17 COSATI CODES			18 SUBJECT TERMS (Continue on reverse if necessary and identify by block number)
FIELD	GROUP	SUB-GROUP	Vortex/Free-Surface Interaction
			Surface Signature

19 ABSTRACT (Continue on reverse if necessary and identify by block number)

Numerical computations have been performed to investigate the interaction of two counter-rotating vortices with a free surface in a viscous, incompressible fluid where the motion is considered two-dimensional and laminar. The decaying vortices deform the free surface during their approach and they can display the phenomenon of "rebounding." The numerical scheme is based on the Navier-Stokes equations and uses boundary-fitted coordinates to accommodate the locally high vorticity of the moving vortices and the nonlinear deformation of the free surface.

20 DISTRIBUTION/AVAILABILITY OF ABSTRACT	21 ABSTRACT SECURITY CLASSIFICATION
☐ UNCLASSIFIED/UNLIMITED ☒ SAME AS RPT ☐ DTIC USERS	UNCLASSIFIED
22a NAME OF RESPONSIBLE INDIVIDUAL	22b TELEPHONE (Include Area Code)	22c OFFICE SYMBOL
Hans J. Lugt	(202) 227-1925	Code 1802

DD Form 1473, JUN 86   Previous editions are obsolete   SECURITY CLASSIFICATION OF THIS PAGE

S/N 0102-LF-014-6603   UNCLASSIFIED

CONTENTS

Page

FIGURES

TABLES

v

ABSTRACT

Numerical computations have been performed to investigate the interaction of two counter-rotating vortices with a free surface in a viscous, incompressible fluid where the motion is considered two-dimensional and laminar. The decaying vortices deform the free surface during their approach and they can display the phenomenon of "rebounding." The numerical scheme is based on the Navier-Stokes equations and uses boundary-fitted coordinates to accommodate the locally high vorticity of the moving vortices and the nonlinear deformation of the free surface.

ADMINISTRATIVE INFORMATION

INTRODUCTION

Two counter-rotating vortices in a two-dimensional viscous fluid approach through self-induction a free surface and interact with it. The fluid is considered incompressible and the laminar flow transient, with the fluid ultimately coming to rest. This scenario may be envisioned as an approximation to a pair of vortex filaments in the far wake of a slowly moving body under water.

Various models of different relevance to this problem can be found in the literature. The classical Lamb solution describes the potential flow generated by a pair of counter-rotating point vortices approaching or leaving a straight boundary. The paths of the vortices are given by

$$x^2 + y^2 = 4x^2y^2 \tag{1}$$

in a Cartesian coordinate system (x, y) with the unit distance between the two vortices far away from the boundary.[1] The behavior of a pair of vortices with an elliptic core was studied by Saffman.[2]

In a viscous fluid an additional boundary condition must be specified for the tangential velocity component. Under nonslip, vorticity of opposite sign to the approaching vortices will be generated, and the paths will be different from that described by Eq. (1). Flow separation can occur at the boundary with the subsequent development of secondary vortices. The primary vortices will turn away from the boundary, a phenomenon that is called "rebounding".[3,4] A numerical computation of the boundary layer at the wall was performed by Ersoy and Walker.[5]

Rebounding was also observed experimentally by Barker and Crow[4] at a water surface. No information, however, was given on the shape of the surface. The vortices were generated by a moving and then abruptly retracted plate in a water tank. Different methods of vortex generation were used by Sarpkaya and Henderson[6] and by Willmarth et al.[7] no studied the

1

disturbance of the water surface in three dimensions by the steady movement of a hydrofoil and by counter-rotating flaps, respectively.

A numerical approach was used by Sarpkaya et al.,[8] Telste,[9] Marcus,[10] and Willmarth et al.[7] for two-dimensional potential flow with two counter-rotating vortices approaching a nonlinear free surface.

The corresponding viscous problem was tackled by Peace and Riley[11] for a plane surface with either a nonslip or a perfect-slip condition. For the initial flow development they used a viscous inner solution and an inviscid outer solution. After this initial phase, a finite-difference scheme for the Navier-Stokes equations was applied.

In this report the viscous-flow problem is solved for a nonlinear free surface which produces vorticity according to the formula: Vorticity equals two times curvature times tangential velocity at the free surface. A finite-difference scheme is used for the entire time span during which the vortices approach the free surface.

STATEMENT OF THE PROBLEM

A pair of vortices of equal strength κ but opposite sign, a distance a apart, approaches through self-induction an initially undisturbed free surface at $y' = 0$ in the Cartesian coordinate system (x', y') (Fig. 1). With the corresponding velocity components u' and v' the time-dependent flow field of the incompressible Newtonian fluid is described by

$$\frac{\partial u'}{\partial t'} + u'\frac{\partial u'}{\partial x'} + v'\frac{\partial u'}{\partial y'} = -\frac{1}{\rho}\frac{\partial p'}{\partial x'} + \nu\left(\frac{\partial^2 u'}{\partial x'^2} + \frac{\partial^2 u'}{\partial y'^2}\right) , \tag{2}$$

$$\frac{\partial v'}{\partial t'} + u'\frac{\partial v'}{\partial x'} + v'\frac{\partial v'}{\partial y'} = -\frac{1}{\rho}\frac{\partial p'}{\partial y'} + \nu\left(\frac{\partial^2 v'}{\partial x'^2} + \frac{\partial^2 v'}{\partial y'^2}\right) -g . \tag{3}$$

$$\frac{\partial u'}{\partial x'} + \frac{\partial v'}{\partial y'} = 0 , \tag{4}$$

with t', p', ρ, ν, and g the time, total pressure, density, kinematic viscosity, and constant of gravity, respectively.

The free surface is described by $y' = Y'(x', t')$ and is part of the solution. On this free surface the boundary conditions are

$$\frac{\partial Y'}{\partial t'} = v' - u'\frac{\partial Y'}{\partial x'} , \tag{5}$$

$$(p' - 2\mu\frac{\partial u'}{\partial x'})\frac{\partial Y'}{\partial x'} + \mu(\frac{\partial u'}{\partial y'} + \frac{\partial v'}{\partial x'}) = 0 \, , \tag{6}$$

$$(p' - 2\mu\frac{\partial v'}{\partial y'}) + \mu(\frac{\partial u'}{\partial y'} + \frac{\partial v'}{\partial x'})\frac{\partial Y'}{\partial x'} = 0 \, . \tag{7}$$

Surface tension is neglected. The other boundary conditions are

$$y' = -\infty \; : \; u' = v' = 0 \, , p' = +\infty \, , \tag{8}$$

$$x' = 0 \, , \; -\infty < y' \leq Y' \; : \; \frac{\partial v'}{\partial x'} = 0 \, , u' = 0 \, , \frac{\partial p'}{\partial x'} = 0 \, , \tag{9}$$

$$x' = +\infty \, , \; -\infty < y' \leq 0 \; : \; u' = v' = 0 \, , p' = -\rho g y' \, . \tag{10}$$

Since the flow field is symmetric about the line $x' = 0$, only the half plane $x' \geq 0$ with one vortex at $x' = x'_v$ and $y' = y'_v$ is considered (Fig. 1).

The following assumptions are made for the initial conditions at $t' = t'_0$:

1. The free surface is undisturbed.

2. A point vortex with strength κ at the position $x' = x'_v$ and $y' = y'_v$ is introduced whose flow field is irrotational and is described in the quadrant $x' \geq 0$, $y' \leq 0$ by

$$\phi' + i\psi' = -i\kappa \log \frac{(z' - z'_v)(z' + z'_v)}{(z' - \overline{z'_v})(z' + \overline{z'_v})} \tag{11}$$

where $z' = x' + iy'$ and ϕ' and ψ' are the potential function and the stream function, respectively.

3. The analytic solution (11) of the flow field does not satisfy the boundary condition (7). This inconsistency has only a small numerical effect on the first few time steps.

4. Since the point vortex represents a singularity with infinite vorticity in the flow field, it is practical to assume a certain decay of the point vortex to accommodate it for a finite-difference grid. If this decay is confined to a local area about the center of the vortex so that there is no appreciable effect on the second vortex, that is, on the symmetry line (or on the free surface), the Hamel-Oseen solution can be applied:[11,12]

$$v'_\varphi = -\frac{\kappa}{r'}[1 - exp(-\frac{r'^2}{4\nu(t' - t'_0)})] \tag{12}$$

with $v'_\varphi = \sqrt{u'^2 + v'^2}$ and $r'^2 = (x' - x'_v)^2 + (y' - y'_v)^2$.

It is convenient to introduce the following dimensionless quantities:

3

$$(x', y', Y') = a(x, y, Y) , \quad t' = \frac{a}{V_0}t , \quad (u', v') = V_0(u, v)$$

$$p' = \rho V_0^2(P - y/Fr^2) , \quad \delta = \frac{H}{a} , \quad V_0 = \frac{\kappa}{a} \tag{13}$$

with H the initial depth of the vortices, V_0 the initial translational velocity of the vortex pair (it may be mentioned that this scaling makes the unit distance in Eq. (1) only approximate, that is, 0.99), and P the scaled dynamic pressure. The dimensionless flow parameters are the Froude and the Reynolds numbers Fr and Re, respectively:

$$Fr^2 = \frac{V_0^2}{ga} = \frac{\kappa^2}{ga^3} , \quad Re = \frac{V_0 a}{\nu} = \frac{\kappa}{\nu} . \tag{14}$$

Moreover, the infinite domain of integration is approximated by a finite domain for numerical reasons. Also, the inertial terms are expressed in conservation form. Then, the initial-boundary value problem is defined by

$$\frac{\partial u}{\partial t} + \frac{\partial u^2}{\partial x} + \frac{\partial(uv)}{\partial y} = -\frac{\partial P}{\partial x} + \frac{1}{Re}\left(\frac{\partial^2 u}{\partial x^2} + \frac{\partial^2 u}{\partial y^2}\right) , \tag{15}$$

$$\frac{\partial v}{\partial t} + \frac{\partial(uv)}{\partial x} + \frac{\partial v^2}{\partial y} = -\frac{\partial P}{\partial y} + \frac{1}{Re}\left(\frac{\partial^2 v}{\partial x^2} + \frac{\partial^2 v}{\partial y^2}\right) , \tag{16}$$

$$\frac{\partial u}{\partial x} + \frac{\partial v}{\partial y} = 0 . \tag{17}$$

with the following boundary conditions:

$$y = Y : \qquad \frac{\partial Y}{\partial t} = v - u\frac{\partial Y}{\partial x} \tag{18}$$

$$\left(P - \frac{Y}{Fr^2} - \frac{2}{Re}\frac{\partial u}{\partial x}\right)\frac{\partial Y}{\partial x} + \frac{1}{Re}\left(\frac{\partial u}{\partial y} + \frac{\partial v}{\partial x}\right) = 0 , \tag{19}$$

$$\left(P - \frac{Y}{Fr^2} - \frac{2}{Re}\frac{\partial v}{\partial y}\right) + \frac{1}{Re}\left(\frac{\partial u}{\partial y} + \frac{\partial v}{\partial x}\right)\frac{\partial Y}{\partial x} = 0 . \tag{20}$$

$y = -y_L : P = 0 , u, v:$ obtained by 2nd-order extrapolation

along coordinate line into the interior , $\tag{21}$

$$x = 0 , -y_L < y \leq Y : \frac{\partial v}{\partial x} = 0 , u = 0 , \frac{\partial P}{\partial x} = 0 , \tag{22}$$

$x = +x_L , -y_L < y \leq 0 : P = 0 , u, v:$ obtained by 2nd-order

extrapolation along coordinate line into the interior . $\tag{23}$

The initial conditions at $t = t_I$ are:

Position of vortex: $x_v = 1/2$, $y_v = -\delta$.

The flow field is irrotational and, according to Eq. (11),

$$\phi + i\psi = -i \log \frac{(z - z_v)(z + z_v)}{(z - \bar{z}_v)(z + \bar{z}_v)} \tag{24}$$

except for the vicinity of the vortex center with the circular boundary r_L:

$$v_{\vartheta} = -\frac{1}{r}[1 - exp(-\frac{r^2 Re}{4(t_L - t_0)})] \ , \ r \leq r_L \ . \tag{25}$$

For a certain r_L, which is determined by the permissible error, t_L can be computed and is for the examples in this report $t_L = 0.125$ with $t_0 = 0$. This t_L is then chosen as the start of the computation: $t = t_L = 0$ with $t_0 = -0.125$.

NUMERICAL TECHNIQUE

The numerical solution of the initial-boundary value problem, as expressed in Eqs. (15) through (25), is carried out with the aid of a finite-difference technique and boundary-fitted coordinates.

Boundary-fitted coordinate transformation

Fig. 1b is a schematic drawing of how the physical space is mapped onto the computational domain. Only the coordinate lines which form the boundaries of the two regions are drawn. The coordinate lines in physical space are mapped onto a uniformly spaced Cartesian mesh with a unit mesh spacing in each coordinate direction.

As the flow field evolves in time, the grid in physical space will move and its coordinate lines will be attracted to regions of high flow gradients through the use of an adaptive-grid technique to be discussed later. However, the Cartesian grid in computational space always remains fixed and uniform. This is the major advantage of using a mapping.

For $Re = 10$, $Fr = 1.125$, the physical region extends from $x = 0$ to 6.0 and from $y = -6.0$ to the free surface which is initially at $y = 0$. This physical region is mapped onto a computational space with a Cartesian grid consisting of 91 equally-spaced points in both the $\xi-$ and $\eta-$ coordinate directions. For the two $Re = 50$ cases, the physical regions extend from $x = 0$ to 10.8 and from $y = -6.0$ to the free surface. These physical regions are mapped onto a computational space with a Cartesian grid consisting of 157 points in the $\xi-$coordinate direction and 135 points in the $\eta-$coordinate direction. Figs. 2 through 4 display representative physical-space grids at various times.

The curvilinear coordinates (ξ, η) are obtained as solutions of the two elliptic partial differential equations with the physical-space coordinates (x, y) as independent variables

$$\xi_{xx} + \xi_{yy} = (\xi_x^2 + \xi_y^2)\, P^*(\xi, \eta) \ , \tag{26}$$

$$\eta_{xx} + \eta_{yy} = (\eta_x^2 + \eta_y^2)\, Q^*(\xi, \eta) \ . \tag{27}$$

However, since all calculations are to be done in the rectangular computational domain, these two elliptic partial differential equations are transformed by interchanging the dependent and independent variables. As a result, the physical-space coordinates (x, y) are solved in terms of the computational space coordinates (ξ, η) at each time step.[13] The transformation yields, with partial derivatives now symbolized by subscripts for simplicity,

$$\alpha x_{\xi\xi} - 2\beta x_{\xi\eta} + \gamma x_{\eta\eta} + \alpha P^* x_\xi + \gamma Q^* x_\eta = 0 \ , \tag{28}$$

$$\alpha y_{\xi\xi} - 2\beta y_{\xi\eta} + \gamma y_{\eta\eta} + \alpha P^* y_\xi + \gamma Q^* y_\eta = 0 \ , \tag{29}$$

with

$$\alpha = x_\eta^2 + y_\eta^2$$

$$\beta = x_\xi x_\eta + y_\xi y_\eta \tag{30}$$

$$\gamma = x_\xi^2 + y_\xi^2 \ .$$

For later use, the Jacobian of the transformation is given by

$$J = x_\xi y_\eta - x_\eta y_\xi \ .$$

The form of the control functions P^* and Q^* for the coordinate system will be presented when adaptive-grid generation is discussed.

The Navier-Stokes equations (15) and (16) are in curvilinear coordinates (ξ, η):[14]

$$u_t - x_t(y_\eta u_\xi - y_\xi u_\eta)/J - y_t(x_\xi u_\eta - x_\eta u_\xi)/J$$

$$+ [y_\eta(u^2)_\xi - y_\xi(u^2)_\eta]/J + [x_\xi(uv)_\eta - x_\eta(uv)_\xi]/J + (y_\eta P_\xi - y_\xi P_\eta)/J$$

$$= (\alpha u_{\xi\xi} - 2\beta u_{\xi\eta} + \gamma u_{\eta\eta} + \sigma^* u_\eta + \tau^* u_\xi)/ReJ^2 \ , \tag{31}$$

$$v_t - x_t(y_\eta v_\xi - y_\xi v_\eta)/J - y_t(x_\xi v_\eta - x_\eta v_\xi)/J$$

$$+ [y_\eta(uv)_\xi - y_\xi(uv)_\eta]/J + [x_\xi(v^2)_\eta - x_\eta(v^2)_\xi]/J + (x_\xi P_\eta - x_\eta P_\xi)/J$$

$$= (\alpha v_{\xi\xi} - 2\beta v_{\xi\eta} + \gamma v_{\eta\eta} + \sigma^* v_\eta + \tau^* v_\xi)/ReJ^2 \ , \tag{32}$$

where

6

$$\sigma^* = \gamma Q^*(\xi, \eta) \; , \quad \tau^* = \alpha P^*(\xi, \eta) \; . \tag{33}$$

The time-derivatives have also been transformed in these equations. Thus, time derivatives in Eqs. (31) and (32) are taken with ξ and η fixed, while those in Eqs. (15) and (16) were taken with x and y fixed. This transformation of time-derivatives allows the computation to be done on a fixed grid in the transformed plane even though the physical grid is in motion due to the movement of the free surface. The terms involving x_t and y_t in Eqs. (31) and (32) hence occur because of the moving physical-space grid. This procedure was adopted from Shanks.[14]

The continuity equation (17) is replaced by an equation with pseudo-compressibility for numerically conserving mass at each physical time step:

$$\frac{\partial P}{\partial \tau} + \beta^* \left(\frac{\partial u}{\partial x} + \frac{\partial v}{\partial y} \right) = 0 \; . \tag{34}$$

In this method pseudo-time steps for pseudo-time τ are required to satisfy Eq. (17) at each physical time step Δt. This approach can be viewed as an iteration procedure in pseudo-time τ to calculate each physical time step Δt. The method has been successfully applied recently by several researchers[15,16] to compute the two-dimensional, incompressible Navier-Stokes equations for time-dependent flows. This technique was first introduced by Chorin[17] for obtaining solutions to the steady-state, incompressible Navier-Stokes equations and is characterized by the existence of moving pseudo-pressure waves. They die out in pseudo-time leaving a divergence-free velocity field at steady state. The method of employing artificial compressibility has been used successfully by many authors for computing steady-state incompressible Navier-Stokes solutions (see, for example, Kwak et al.[18]).

The parameter β^* can assume values between zero and ten but is usually chosen to be one, and so it is in the present work. Then, Eq. (34) is in the transformed computational space

$$\frac{\partial P}{\partial \tau} + \frac{1}{J}(y_\eta u_\xi - y_\xi u_\eta + x_\xi v_\eta - x_\eta v_\xi) = 0 \; . \tag{35}$$

The movement of the grid during the pseudo-time step $\Delta \tau$ is so small that the terms involving x_τ and y_τ have been neglected in Eq. (35).

The kinematic boundary condition (18) at the free surface is for coordinates in computational space

$$y = Y: \quad \left(\frac{\partial Y}{\partial t} \right)_x = v - u \frac{Y_\xi}{x_\xi} \; . \tag{36}$$

The subscript x refers to the physical space grid points at the free surface that are not permitted to move in the x-direction. An equivalent kinematic condition to Eq. (36) is given in the following equation in which the grid points at the free surface are allowed to move in the x-direction:

$$y = Y: \quad \frac{\partial Y}{\partial t} = v \; , \quad \frac{\partial x}{\partial t} = u \; . \tag{37}$$

7

Both equivalent kinematic conditions (36) and (37), of course, permit the grid points at the free surface in physical space to move in the y-direction.

The free surface in physical space maps onto a constant η-line in computational space, as seen in Fig. 1b. For a constant η-line, the free surface conditions (19) and (20), written in computational-space coordinates, are

$$y = Y: \quad u_\eta = \frac{1}{\gamma}[Ju_\xi - Jv_\xi - ReJy_\xi(P - \frac{Y}{Fr^2})] \ , \tag{38}$$

$$v_\eta = \frac{1}{\gamma}[Ju_\xi + Jv_\xi + ReJx_\xi(P - \frac{Y}{Fr^2})] \ . \tag{39}$$

In addition to the kinematic condition for Y at the free surface, three conditions are needed to determine P, u, and v at the free surface. Condition (38) is retained to compute u whereas a linear combination of Eqs. (38) and (39) is derived that yields the condition for P. The velocity component v is then obtained from the continuity equation to conserve mass at the free surface. The conditions for P and v at the free surface $y = Y$ are

$$P = \frac{Y}{Fr^2} + \frac{1}{ReJ}(x_\xi v_\eta - y_\xi u_\eta) - \frac{1}{\gamma Re}[u_\xi x_\xi + v_\xi y_\xi + \frac{\beta}{J}(v_\xi x_\xi - u_\xi y_\xi)] \tag{40}$$

$$y_\eta u_\xi - y_\xi u_\eta + x_\xi v_\eta - x_\eta v_\xi = 0 \ . \tag{41}$$

At $x = 0$, the symmetry conditions (22), after being written in computational-space coordinates, are used to compute v from the Navier-Stokes equation (32) and P from Eq. (35). The y-coordinate at $x = 0$ is obtained from Eq. (29). Of course, u and x are always zero on the symmetry line $x = 0$, including the symmetry point at the free surface. At this special point, Y, P, and v are obtained from Eqs. (36), (40), and (41), respectively, with the symmetry conditions (22) built in.

The boundary conditions (21) and (23) are used with second-order extrapolations along interior coordinate lines in computational space to obtain u and v at these boundaries. For instance, at $y = -y_L$, u is obtained from values of u at the two grid points on a constant ξ-line closest to the boundary. Similar considerations apply to v and to the boundary of Eq. (23), except that constant η-lines are used there.

Adaptive gridding is used in this report by giving a special form to the coordinate-system control functions P^*, Q^*, which appear in Eqs. (28), (29), (31), and (32). The basic idea is to use the equi-distribution of a weight function along arclength elements in the physical-space grid.[19] These equi-distribution laws for weight functions w_1 and w_2 along arclength elements on constant η- and ξ-lines, respectively, are

$$(x_\xi^2 + y_\xi^2)^{\frac{1}{2}} w_1 = const \ , \tag{42}$$

$$(x_\eta^2 + y_\eta^2)^{\frac{1}{2}} w_2 = const \ . \tag{43}$$

Weight functions are usually taken to be functions of the flow gradient, and they are chosen here to be

$$w_1 = (1 + B^2 \mid \frac{q_{\xi\xi}}{(1 + q_\xi^2)^{3/2}} \mid) \sqrt{1 + A^2 q_\xi^2} \tag{44}$$

$$w_2 = (1 + B^2 \mid \frac{q_{\eta\eta}}{(1 + q_\eta^2)^{3/2}} \mid) \sqrt{1 + A^2 q_\eta^2} \; , \tag{45}$$

where $q = \sqrt{u^2 + v^2}$.

One observes from Eqs. (42) through (45) that the spacing of the arclength between grid points in physical space will be small if the gradient of the local flow speed q is high. The grid adapts to the locally high flow gradient. If the local flow gradient is zero, uniform spacing will occur.

Anderson[19] has shown that if P^* and Q^* have the form

$$P^* = \frac{(w_1)_\xi}{w_1} \; , \quad Q^* = \frac{(w_2)_\eta}{w_2} \; , \tag{46}$$

the mesh-generating equations (28) and (29) approximate the equi-distribution laws (42) and (43), respectively. In the computations, coefficients C_1 and C_2 are actually added to the right sides of Eq. (46). C_1 and C_2, which are constant in time but vary spatially, are the initial P^* and Q^*, respectively, for the initial, non-uniform Cartesian grid in physical space obtained from the INMESH program.[20] This grid is used at the very start of the flow computation at $t = 0$ with adaptive gridding then applied immediately.

On the symmetry line $x = 0$, the weight function w_2 is given in the simpler form

$$w_2 = 1 + A v_\eta^2 \; . \tag{47}$$

Only Q^* in Eq. (46) and Eq. (47) are required in conjunction with Eqs. (29) and (32) to compute y and v, respectively, on the symmetry line $x = 0$.

Except for the symmetry line, adaptive gridding is used only in the interior of the flow region.

Finite-Difference Technique

All spatial derivatives, including one-sided derivatives at the boundaries, are replaced by finite-difference operators of second order in the computational space. Thus, it remains to discuss only the implicit time-differencing procedure for the initial-boundary value problem that consists of Eqs. (21) through (25), (28) through (33), (35), (36) or (37), (38), (40), (41), and (46). The weight functions in Eq. (46) are provided by Eqs. (44), (45) or (47).

The dynamic pressure field P at $t = t_L = 0$ is obtained by solving a Poisson equation for P in terms of the initial velocity field, Eqs. (24) and (25). This is the only time a Poisson equation for P is used.

The following equations represent the implicit time differencing procedure for advancing the flow solution (P, u, v, x, y) in the interior for the physical time step $\Delta t = t^{n+1} - t^n$ from physical time level n to level $n + 1$ by using pseudo-time steps $\Delta \tau = \tau^{m+1} - \tau^m$:

$$x^{n+1, m+1} = g_1(x^{n+1, m+1}, y^{n+1, m+1}, P^{*n}, Q^{*n}) , \tag{48}$$

$$y^{n+1, m+1} = g_2(x^{n+1, m+1}, y^{n+1, m+1}, P^{*n}, Q^{*n}) . \tag{49}$$

$$\frac{P^{n+1, m+1} - P^{n+1, m}}{\Delta \tau} = -(\nabla \cdot \vec{V})^{n+1, m+1} . \tag{50}$$

$$\frac{u^{n+1, m+1} - u^n}{\Delta t} = r_1^{n+1, m+1} . \tag{51}$$

$$\frac{v^{n+1, m+1} - v^n}{\Delta t} = r_2^{n+1, m+1} . \tag{52}$$

Eqs. (48) through (52) are obtained from Eqs. (28), (29), (35), (31), and (32), respectively. Superscripts refer to time levels. The nonlinear functions g_1 and g_2 in Eqs. (48) and (49) are functions of the latest updated values $x^{n+1, m+1}$, $y^{n+1, m+1}$ at the neighboring points after using spatial differencing. In Eqs. (51) and (52) the time derivatives for u and v are on the left side of the equations while all remaining terms of Eqs. (31) and (32) (in difference form) are included in the functions r_1 and r_2 on the right side of Eqs. (51) and (52). Physical time derivatives occur in Eqs. (31), (32), (36) or (37) and are differenced to first order according to

$$f_t = \frac{f^{n+1, m+1} - f^n}{\Delta t} , \tag{53}$$

where f stands for u, v, x, y, or Y. All spatial derivatives of the initial-boundary value problem, after second-order finite differencing, are evaluated by using the latest available updated values of the implicit scheme.

The flow solution at the new physical time level $n + 1$ is obtained when the convergence criteria

$$|f^{n+1, m+1}| > \epsilon_1 , \tag{54}$$

$$\left| \frac{f^{n+1, m+1} - f^{n+1, m}}{f^{n+1, m}} \right| < \epsilon_2 \tag{55}$$

are satisfied for $f = u$, v, x, and y at all grid points of the computational space. Then, $f^{n+1} = f^{n+1, m+1}$. In Eqs. (54) and (55) ϵ_1 and ϵ_2 are small specified parameters.

Rogers and Kwak[15] used the implicit scheme of Eqs. (50) through (52) for flow problems with fixed geometry. Eqs. (51) and (52) can be viewed as an Euler backward scheme for the Navier-Stokes equations. The convergence of P in pseudo-time ensures conservation of mass at each physical time step as

discussed earlier. This process is also seen from Eq. (50).

Rogers and Kwak[15] used upwind differencing for the convective terms of Eqs. (51) and (52) which is necessary for high Reynolds numbers. In this work a central difference operator was applied.

A "four-color" scheme (Fig. 1c) is used in the interior of the computational space for Eqs. (48) and (49) and for Eqs. (50) through (52) in obtaining the latest values with superscripts $n+1$, $m+1$ (updates) for x, y and P, u, and v, respectively. The use of such a scheme, which can be vectorized, resulted in an order of magnitude increase in computer speed on the Cray-XMP 24 on which the computations were performed.

The "four-color" scheme, as applied to Eqs. (50) through (52), for example, consists of obtaining updates for P, u, v simultaneously at all the o points, then at all the points, the x points, and the $\triangle$ points, in that order. The latest available updates are used in this process.

The computational cycle for one complete pseudo-time step iteration consists of (a) applying the "four-color" scheme to Eqs. (48) and (49) followed by obtaining the latest updates for y at successive points along the symmetry boundary Eq. (22) from Eq. (49); (b) applying the "four-color" scheme to Eqs. (50) through (52); (c) obtaining updates for P and v at successive points along the symmetry boundary Eq. (22) from Eqs. (50) and (52), respectively; (d) obtaining updates for P, u, v, and Y at successive points along the free surface from Eqs. (40), (38), (41), and (36), respectively; and (e) obtaining updates for u and v at successive points, first along the boundary $x = x_L$ from Eq. (23) and then along the boundary $y = -y_L$ from Eq. (21).

At the completion of this computational cycle, after the latest updates for x, y, u, and v satisfy the convergence criteria of Eqs. (54) and (55) at all points, these updates are the solution at the new time level $n + 1$. If the convergence criteria are not met, cycle (a) through (e) is repeated until they are met.

In this report a spatially varying pseudo-time step $\Delta\tau$ is used that can be interpreted as an attempt to use a more uniform pseudo-Courant number throughout the field.[21] A spacially varying $\Delta\tau$ can be effective for physical-grid spacings that vary from very fine to very coarse grids, a situation which particularly occurs for the two $Re = 50$ cases. Pulliam and Steger[21] mention that a spatially varying physical-time step Δt has been used by a number of researchers to obtain solutions of steady-state compressible fluid flows. Gorski[22] applies a spatially varying pseudo-time step for obtaining solutions of steady-state incompressible fluid flows. It appears logical, therefore, that in this study, which obtains the solution of a "steady-state" incompressible fluid flow at each physical time step Δt by marching through pseudo-time steps $\Delta\tau$, a spatially varying pseudo-time step $\Delta\tau$ be used. This time step, used in Eq. (50), is

$$\Delta\tau = \frac{J^2 \cdot \Delta\tau_{ref}}{\alpha + \gamma} \tag{56}$$

11

and scales directly with the area and aspect ratio of a physical grid cell ($|J|$ is the area of a cell in physical space). The value of the parameter $\Delta\tau_{ref}$ will be given later.

The form of Eq. (56), given by Hodge,[23] is borrowed from Thompson and Shanks (Appendix D)[13] where it appears somewhat disguised in a discussion relating the artificial-compressibility procedure and a Poisson equation for the pressure.

Thompson and Shanks,[13] who solved the time-dependent, two-dimensional Navier-Stokes equations for the viscous fluid flow about a hydrofoil at a free surface, used artificial compressibility to obtain the pressure at the free surface and the hydrofoil, and they employed a Poisson equation for the pressure in the interior of the flow region. In the present report, in contrast, artificial compressibility is used to obtain the pressure in the interior of the flow region, and boundary conditions for the pressure are used to obtain the pressure at the free surface and other boundaries.

For the case $Re = 50$, $Fr = 0.356$ only, a free surface instability developed at $t = 3.52$. Starting at this time, upon convergence at each new physical time (level $n + 1$), the values for $f = u$, v, P, Y at the free surface point i are finally given in terms of their corresponding converged values $\hat{f}$:

$$f_i = \frac{1}{16}(-\hat{f}_{i+2} - \hat{f}_{i-2} + 4(\hat{f}_{i+1} + \hat{f}_{i-1}) + 10\hat{f}_i) \; . \tag{57}$$

This filtering process was developed by Shapiro[24] and was used by Longuet-Higgins and Cokelet,[25] among others, to eliminate numerical instability at the free surface. For $Re = 50$, $Fr = 0.356$, filtering was applied at the free surface from $x = 1.0$ to 2.0 during the time $t = 3.52$ to 4.75 and from $x = 1.0$ to 2.94 during the time $t = 4.75$ to 9.52.

The kinematic condition (36) was used for all cases except $Re = 50$, $Fr = 1.125$ from $t = 2.40$ to 4.06. During that time Eq. (37) was used because of the need to crowd more free-surface points in the x-direction to resolve the steep wave generated for this case.

The relaxation factors were chosen to be 1.85 for Eqs. (48) and (49) and 1.0 for Eqs. (51) and (52). The parameters $(\epsilon_1, \epsilon_2) = (0.01, 0.01)$ were applied to Eqs. (48) and (49) and $(\epsilon_1, \epsilon_2) = (0.03, 0.01)$ to Eqs. (51) and (52).

The adaptive grid parameters $(A, B) = (2.0, 2.0)$ were used for all cases except $Re = 50$, $Fr = 1.125$ from $t = 3.10$ to 4.06. During this time, (A, B) were gradually increased to $(3.8, 3.8)$.

For the two $Re = 50$ cases, the parameters $(\Delta t, \Delta\tau_{ref})$ were gradually increased from $(10^{-8}, 460.8)$ to $(0.0003, 2560)$ during the time $t = 0$ to 0.019. For these two cases, the parameters $(\Delta t, \Delta\tau_{ref}) = (0.0003, 2560)$ did not change for the remainder of their time histories, except that Δt was cut back to 0.00015 for $Fr = 0.356$ from $t = 3.52$ to 5.02 and that the parameter set $(0.0003, 2560)$ for $Fr = 1.125$ was reduced to $(0.000025, 1920)$ from $t = 4.0$ to 4.06. The total time span extends to $t = 9.52$ and $t = 4.06$ for $Fr = 0.356$ and $Fr = 1.125$, respectively.

12

For $Re = 10$, $Fr = 1.125$, the spatially varying pseudo-time step $\Delta \tau$ was not used because the grid in physical space remained more uniform in time than it did in the other cases, since the flow gradients are smaller for the case $Re = 10$ than for the other cases. For $Re = 10$ the parameters $(\Delta t, \Delta \tau)$ were gradually increased from $(10^{-5}, 1.6)$ to $(0.00015, 8.0)$ during the time $t = 0$ to 0.007. The parameters $(0.00015, 8.0)$ were then retained until the end at $t = 9.04$.

For the two $Re = 50$ cases a maximum of three to eight pseudo-time step iterations per physical time step near $t = 0$ were needed. Iterations for $Fr = 0.356$ then gradually leveled off to one to two iterations per physical-time step for the remainder of the time. Iterations for $Fr = 1.125$ leveled off to two but then increased to two to five iterations per physical-time step as the wave steepened. The $Re = 10$ case required fewer iterations per physical-time step than the $Re = 50$ cases.

Mass conservation was monitored in the flow field for the three flow cases. The details are here omitted.

The computer time used on the Cray-XMP 24 for $Re = 50$, $Fr = 0.356$ and $Re = 50$, $Fr = 1.125$, which were run until $t = 9.52$ and 4.06, respectively, were approximately 140 and 65 minutes, respectively. $Re = 10$, which was run until $t = 9.04$, needed 75 minutes.

To build confidence in the numerical method used, the case of $Re = 50$, $Fr = 0.356$ was also computed with a grid which had four times the number of cells of the original grid, that is, (313×269) points. The results, which are discussed later, agree quite well with those of the coarser grid of (157×135) points.

The relationship among $\Delta \tau_{ref}$, Δt, the fineness of the grid, and the convergence criteria still must be explored for maximum efficiency and accuracy of the numerical method used in this work.

An auxiliary quantity of interest in the generation of vorticity at the free surface is the distribution of surface vorticity ω_s. For a given free surface $y = Y(x, t)$ and surface velocity components u_s and v_s, the surface vorticity is given by the well-known formula "twice the surface curvature times tangential velocity", or in this report's notation

$$\omega_s = \frac{2 Y_{xx}}{(1 + Y_x^2)^2} (u_s + Y_x v_s) , \qquad (58)$$

In computational space, Y_x and Y_{xx} must be replaced by

$$Y_x = \frac{Y_\xi}{x_\xi} , \quad Y_{xx} = \frac{Y_{\xi\xi} - \frac{Y_\xi}{x_\xi} x_{\xi\xi}}{(x_\xi)^2} . \qquad (59)$$

Numerically, an alternative way of computing ω_s can be chosen by the definition of $\omega = \partial v / \partial x - \partial u / \partial y$ itself. Since in this case information from the interior points is incorporated into the numerical scheme, the result appears more accurate than with the use of Eq. (58) in which Y_{xx} appears, a

13

quantity difficult to obtain with sufficient accuracy. In Fig. 5 the discrepancy between the two methods is shown for the special case $Re = 50$, $Fr = 0.356$ at $t = 5.02$ for both the coarser and the finer grids. A decision as to which formula is more accurate cannot yet be made.

RESULTS

Numerical computations were performed for $Re = 10$ and 50, $Fr = 1.125$, and for $Re = 50$, $Fr = 0.356$ from the initial position $x_v = 0.5$, $y_v = -\delta = -3$. The Froude numbers were selected to coincide with those of Sarpkaya et al.[8] and Telste.[9]

In the case of $Re = 10$, $Fr = 1.125$ diffusion dominates convection so much (the fluid is so "viscous") that the maximum elevation $y = 0.307$ at $t = 4.0$ caused by the vortex motion is small compared to the corresponding inviscid-flow case of Sarpkaya et al.[8] and Telste.[9] The free surface returns, after the maximum elevation has been reached, monotonically to the state at rest. Fig. 6 displays the vector field of the velocity at $t = 4.0$, and Figs. 7 and 8 show equi-vorticity lines at $t = 4.48$ and $t = 9.04$. The vorticity distribution on the free surface is seen in Fig. 9. The data for the positions of the vortex are recorded in Table 1. The path is plotted in Fig. 10 and compared with the solution for the potential flow with a flat surface, Eq. (1). In viscous flow, the center of the vortex can be defined either as the place of extremal vorticity (in this case of minimum vorticity) or as the center of the whirl (center of the nested streamlines). The latter definition, however, depends on the choice of the reference frame. In Fig. 6 the reference frame is fixed to the undisturbed free surface and the vortex is moving relative to this frame. If the reference frame is fixed to the vortex center, the position of the center of the whirl (moving relative to the reference frame) shifts closer to that of the minimum vorticity (see next paragraph for an example). Even then, these two locations do not necessarily coincide as the analytical solution for a decaying vortex dipole demonstrates.[26] Fig. 10 shows that the path of the point of minimum vorticity is closer to the axis of symmetry and closer to the free surface than the path of the whirl's center. The phenomenon of "rebounding" is observed in both cases, that is, the turning away of the vortex from the free surface. The elevated surface returns to the state at rest without oscillation. At the last computed time $t = 9.04$, $|\omega_{min}|$ is 0.2383, diminished from the initial value $|\omega_{min}| = 39.43$. In Fig. 11 $|\omega_{min}|$ is plotted against time. The curve follows closely the $1/t$-decay according to the Hamel-Oseen solution, Eq. (25), indicating that numerical diffusion is minimal.

For $Re = 50$, $Fr = 1.125$ the situation is quite different. The surface elevations at three different times in Figs. 12 through 16 reveal a much stronger effect of the ascending vortex, and a local depression of the surface, called a "scar" by Sarpkaya and Henderson,[6] is now visible that was not apparent in the case of $Re = 10$, $Fr = 1.125$. The surface elevations for $Re = 50$, $Fr = 1.125$ are closer to the curves for the inviscid fluid. In fact, Figs. 12, 15, and 16 may be compared with Figs. 5a, 5c, and 5e of Sarpkaya et al.[8] The dimensionless time T in their work is related to this report's time t by $T = t - 3$. Although it takes a little longer for the viscous fluid flow to reach

14

states comparable to those of the inviscid fluid, the qualitative agreement between the two cases is good with regard to free-surface height at the centerline and the locations of whirl center and scar. The same statement can be made about Telste's data.[9] They can be compared with those in this report, if one considers the relation between the dimensionless time t_{Telste} and t to be $t_{Telste} = 2\pi(t + 2)$. The Froude numbers are related by $Fr_{Telste} = 2\pi Fr$.

In Figs. 13 and 14 a section of the flow field of Fig. 12 is compared for two reference frames. The reference frame fixed to the center of the whirl (Fig. 14) shows that the center is shifted to the left, but the new center does not reach the location of $|\omega'_{min}|$. The equi-vorticity lines are displayed in Figs. 17 through 19. The merger of the vorticity field of the vortex with that at the free surface is clearly visible. The vorticity distribution on the free surface is given in Fig. 20. The path of the vortex center is plotted in Fig. 21 and the positions of the vortex center put together in Table 2. The movement of the vortex is straight up and no deflection due to the free surface is observed. The decrease of $|\omega'_{min}|$ with time is given in Fig. 22 and follows the $1/t$-law. The computations were stopped at $t = 4.06$ when convergence thereafter could not be obtained for the grid used. However, a negative horizontal velocity component at the free surface indicates that the trend toward a constriction is present, as it is in the case of the inviscid fluid. The mounded shape of the free surface around the symmetry line was still rising when the computation was terminated.

A comparison of Fig. 20 with Fig. 22 shows that the surface vorticity becomes larger than $|\omega'_{min}|$ of the vortex from approximately $t = 4$ on. This is an interesting situation because it means that the vorticity concentration of the flow-generating vortices is less than the surface vorticity generated by the vortices. The statement contrasts the result obtained for the flat slip-surface by Peace and Riley,[11] that the flat surface is always a sink of positive vorticity (or a source of negative vorticity) because $\omega'_s = 0$.

The final case computed was $Re = 50$, $Fr = 0.356$. The lower Froude number means less disturbance of the free surface by the vortex motion. This smaller disturbance is observed in Figs. 23 through 25. On the centerline the free surface reaches a maximum elevation, then falls to a minimum, climbs again to a maximum, and comes to the state at rest. In other words, the free surface oscillates. This oscillation is in contrast to the case of $Re = 10$, $Fr = 1.125$ that showed only an up and down movement of the free surface at the center line. The scar is now pronounced, with the high surface curvature that results in high surface vorticity (Figs. 26 through 31). From this concentration of vorticity a secondary vortex develops which becomes visible at $t = 5.02$ in front of the primary vortex (Fig. 28). This figure was also computed with the finer (313×269) grid in Fig. 29. The two figures agree well except for the low-level positive values. A little later, at $t = 6.52$, the secondary vortex has placed itself directly in front of the primary vortex farther away from the free surface (Fig. 30). The computations were continued without any numerical difficulties and were stopped at $t = 9.52$. In Fig. 32 the free-surface vorticity is displayed, and in Fig. 33 the path of the vortex center. In Table 3 the position data are recorded. In contrast to the previous case of $Re = 50$, $Fr = 1.125$, the path of the vortex center now

shows a rebound from the free surface. The decrease of $|\omega_{min}|$ with time is shown in Fig. 34. The agreement between the curves in Figs. 22 and 34 is very good, and the $1/t$-law is observed. This means that the decay of the vortex-center vorticity is not influenced, or barely so, by the presence of the free surface. Here again, the data are compared with those for the finer grid, and almost no distinction can be observed.

The velocity field in Fig. 23 can be compared with that for an inviscid fluid as shown by Telste.[9] The scars are less pointed in the case of a viscous fluid than in the case of an inviscid one, and the position of the vortex center is lower in the viscous-flow case than in the inviscid-fluid one.

The influence of surface tension, the case of an oblique approach of a vortex pair toward the free surface, and an attempt to compute flows with higher Reynolds number will be treated in a forthcoming paper.

ACKNOWLEDGMENT

REFERENCES

1. Lamb, H., "Hydrodynamics," Dover, New York (6th ed.) 1945.

2. Saffman, P.G., "The Approach of a Vortex Pair to a Plane Surface in Inviscid Fluid," J. Fluid Mech., 92, 497 (1979).

3. Harvey, J.K. and F.J. Perry, "Flow Field Produced by Trailing Vortices in the Vicinity of the Ground," AIAA J., 9, 1659 (1971).

4. Barker, S.J. and S. C. Crow, "The Motion of Two-Dimensional Vortex Pairs in a Ground Effect," J. Fluid Mech., 82, 659 (1977).

5. Ersoy, S. and J.D.A. Walker, "Viscous Flow Induced by Counter-Rotating Vortices," Physics of Fluids, 28, 2687 (1985).

6. Sarpkaya, T. and D.O. Henderson, "Surface Disturbances due to Trailing Vortices," Naval Postgraduate School Rep. NPS-69-84-004, Monterey, CA, March 1984.

7. Willmarth, W.W., G. Tryggvason, A. Hirsa, and D. Yu, "Vortex Pair Generation and Interaction With a Free Surface," Physics of Fluids A, 1, 170 (1989).

8. Sarpkaya, T., J. Elnitsky II, and R.E. Leeker, Jr., "Wake of a Vortex Pair on the Free Surface," 17th Symp. on Naval Hydrodynamics, The Hague, Aug. 29-Sep 2, 1988.

9. Telste, J.G., "Potential Flow About Two Counter-Rotating Vortices Approaching a Free Surface," J. Fluid Mech., 201, 259 (1989).

10. Marcus, D.L., "The Interaction Between a Pair of Counter-Rotating Vortices and a Free Boundary," PhD thesis, University of California at Berkeley, 1988.

11. Peace, A.J. and N. Riley, "A Viscous Vortex Pair in Ground Effect," J. Fluid Mech., 129, 409 (1983).

12. Ting, L., "Studies on the Motion and Decay of a Vortex Filament," Lecture Notes in Physics 148, Springer-Verlag, 67 (1981).

13. Thompson, J.F. and S.P. Shanks, "Numerical Solution of the Navier-Stokes Equations for 2d Surface Hydrofoils," Mississippi State University Rep. MSSU-EIRS-ASE-77-4, Feb. 1977.

14. Shanks, S.P., "Numerical Simulation of Viscous Flow about Submerged Arbitrary Hydrofoils using Non-orthogonal, Curvilinear Coordinates," Ph.D. Dissertation, Mississippi State University, Mississippi 1977.

15. Rogers, S.E. and D. Kwak, "An Upwind Differencing Scheme For the Time-Accurate Incompressible Navier-Stokes Equations," AIAA Paper 88-2583, 1988.

16. Merkle, C.L. and M. Athavale, "Time-Accurate Unsteady Incompressible Flow Algorithms Based on Artificial Compressibility," AIAA Paper 87-1137, 1987.

17. Chorin, A.J., "A Numerical Method for Solving Incompressible Viscous Flow Problems," J. Comp. Phys., 2, 12 (1967).

18. Kwak, D., J.L.C. Chang, S.P. Shanks, and S.R. Chakravarthy, "A Three-Dimensional Incompressible Navier-Stokes Flow Solver Using Primitive Variables," AIAA J. 24, 390 (1986).

19. D.A. Anderson, "Constructing Adaptive Grids with Poisson Grid Generators" in: Numerical Grid Generation in Computational Fluid Dynamics, edited by J. Häuser, C. Taylor. Pineridge Press, Swansea, U.K., p. 125, 1986.

20. Coleman, R.M., "INMESH: An Interactive Program for Numerical Grid Generation," Report DTNSRDC-85/054, 1985.

21. Pulliam, T.H. and J.L. Steger, "Recent Improvements in Efficiency, Accuracy, and Convergence for Implicit Approximate Factorization Algorithms," AIAA Paper 85-0360, 1985.

22. Gorski, J.J., "TVD Solution of the Incompressible Navier-Stokes Equations With an Implicit Multigrid Scheme," AIAA Paper 88-3699, 1988.

23. Hodge, J.K., "Numerical Solution of Incompressible Laminar Flow about Arbitrary Bodies in Body-Fitted Curvilinear Coordinates," Ph.D. Dissertation, Mississippi State University, Mississippi 1975.

24. Shapiro, R., "Linear Filtering," Math. Comp., 29, 1094 (1975).

25. Longuet-Higgins, M.S. and E.D. Cokelet, "The Deformation of Steep Surface Waves. I. A Numerical Method of Computation," Proc. Roy. Soc. London A 350, 1 (1976).

26. Lugt, H.J., "Multipole Decomposition of Solutions of the Vector Diffusion Equation," SIAM J. Appl. Math., 39, 264 (1980).

Table 1

Positions x, y of $|\omega_{min}|$ and center of whirl as a function of time t for $Re = 10$, $Fr = 1.125$.

| | $|\omega_{min}|$ | | whirl | |
t	x	y	x	y
0.0	0.50000	-3.00000		
0.16	0.53240	-2.87100		
0.52	0.53950	-2.56443	0.72	-2.61
1.00	0.59450	-2.23920	0.84	-2.37
1.48	0.64670	-2.07500	0.95	-2.20
2.02	0.74830	-1.91060	1.08	-2.02
2.50	0.79907	-1.79872	1.17	-1.92
3.04	0.84954	-1.68650	1.24	-1.86
3.52	0.95000	-1.63019	1.32	-1.82
4.00	1.00017	-1.52198	1.39	-1.79
4.48	1.05031	-1.52026	1.44	-1.84
5.02	1.15026	-1.47129	1.50	-1.94
5.50	1.20021	-1.47590	1.54	-1.90
6.04	1.25013	-1.43300	1.58	-1.93
6.52	1.34996	-1.44439	1.59	-1.95
7.00	1.39995	-1.50670	1.68	-2.04
7.54	1.44993	-1.52009	1.70	-2.04
8.02	1.49997	-1.58206	1.75	-2.14
8.50	1.54994	-1.59290	1.78	-2.12
9.04	1.60000	-1.65366	1.79	-2.16

Table 2

Positions x, y of $|\varsigma'_{min}|$ and center of whirl as a function of time t for $Re = 50$, $Fr = 1.125$.

	$|\varsigma'_{min}|$		whirl	
t	x	y	x	y
0.0	0.5000	-3.0000		
0.007	0.5079	-2.9920		
0.019	0.5056	-2.9861		
0.040	0.5048	-2.9616		
0.160	0.5077	-2.8419		
0.520	0.5159	-2.4853	0.55	-2.50
1.000	0.5235	-2.0527	0.58	-2.06
1.480	0.5262	-1.6196	0.62	-1.64
2.020	0.5280	-1.1672	0.65	-1.19
2.401	0.5604	-0.8926	0.66	-0.91
2.500	0.5367	-0.8115	0.68	-0.83
3.040	0.5558	-0.4561	0.70	-0.49
3.100	0.5705	-0.4207	0.71	-0.46
3.520	0.5677	-0.2185	0.70	-0.23
3.920	0.5751	-0.0803	0.68	-0.13
3.940			0.68	-0.08
4.000	0.5798	-0.0249	0.68	-0.05
4.050	0.5890	-0.0284		
4.060	0.5909	-0.0265	0.66	-0.04

Table 3

Positions x, y of $|\omega_{min}|$ and center of whirl as a function of time t for $Re = 50$, $Fr = 0.356$.

	$|\omega_{min}|$		whirl	
t	x	y	x	y
0.0	0.5000	-3.0000		
0.007	0.5079	-2.9920		
0.019	0.5056	-2.9861		
0.040	0.5048	-2.9616		
0.160	0.5077	-2.8419		
0.520	0.5159	-2.4854	0.55	-2.50
1.000	0.5238	-2.0557	0.58	-2.04
1.490	0.5272	-1.6353	0.62	-1.65
2.020	0.5608	-1.2605	0.66	-1.28
2.500	0.6255	-0.9778	0.71	-1.03
3.040	0.7208	-0.7876	0.80	-0.88
3.520	0.9058	-0.7160	0.92	-0.85
3.760	0.9999	-0.7288	1.01	-0.85
4.000	1.1247	-0.7406	1.10	-0.88
4.240	1.2189	-0.7796	1.20	-0.90
4.480	1.3439	-0.7836	1.32	-0.92
4.750	1.4379	-0.8160	1.42	-0.93
5.020	1.5314	-0.8454	1.50	-0.94
5.500	1.6566	-0.8678	1.64	-0.96
6.040	1.7811	-0.8855	1.75	-0.96
6.520	1.8752	-0.8716	1.84	-0.98
7.000	1.9690	-0.8950	1.94	-1.00
7.540	2.0942	-0.8903	2.06	-1.00
8.020	2.1881	-0.8924	2.14	-1.00
8.500	2.2820	-0.8995	2.24	-1.02
9.040	2.3760	-0.9107	2.33	-1.06
9.520	2.4701	-0.9211	2.43	-1.08
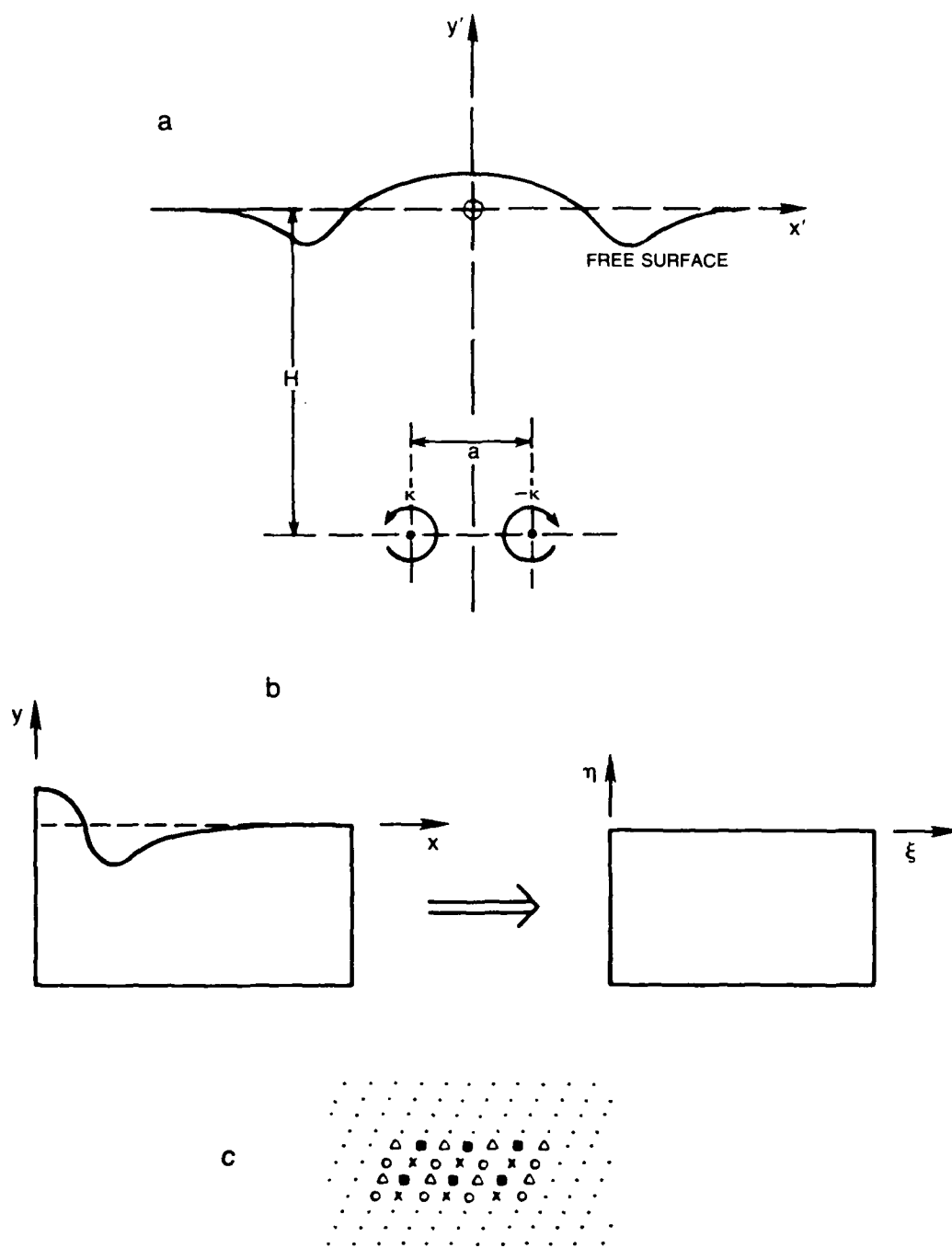
Fig. 1. (a) Sketch of the flow situation. (b) Mapping of the physical space onto the computational space. (c) "Four-color" scheme.
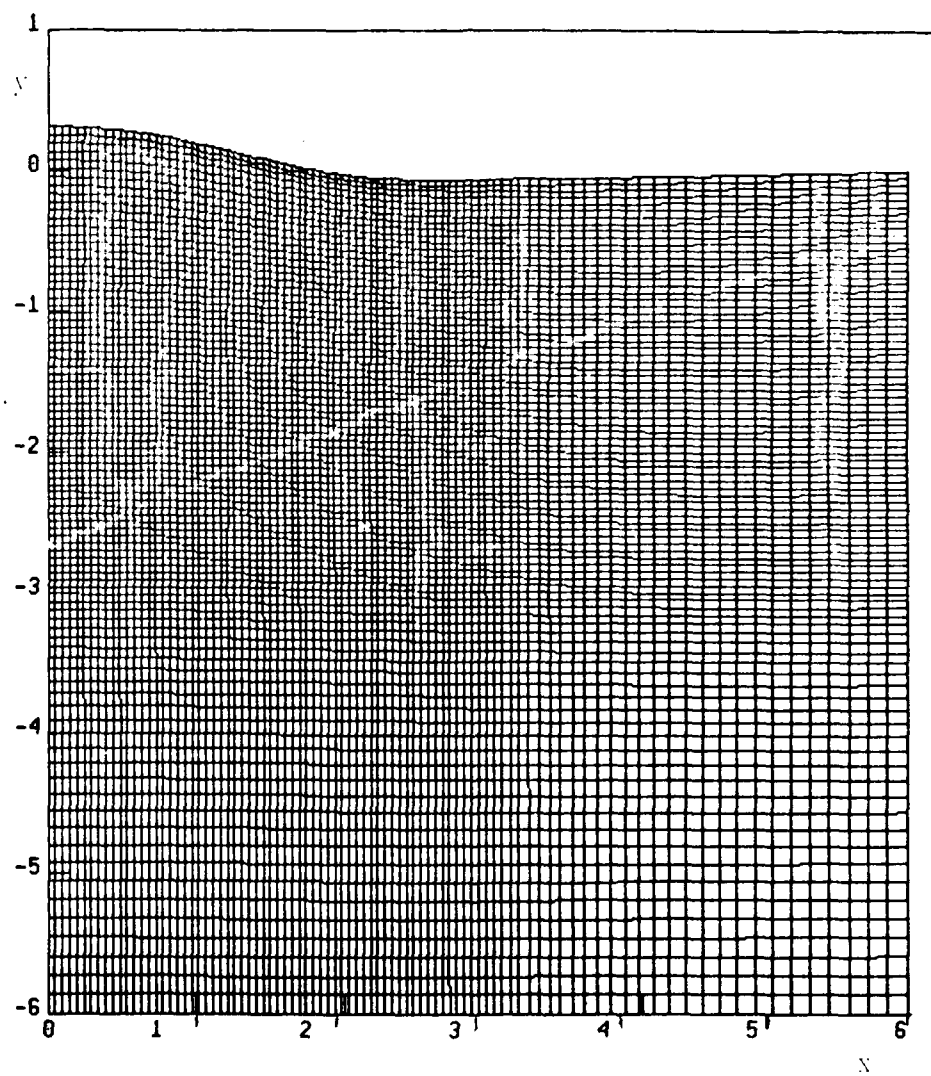
Fig. 2. Grid of the computational half-plane for $Re = 10$, $Fr = 1.125$, $t = 4.0$.
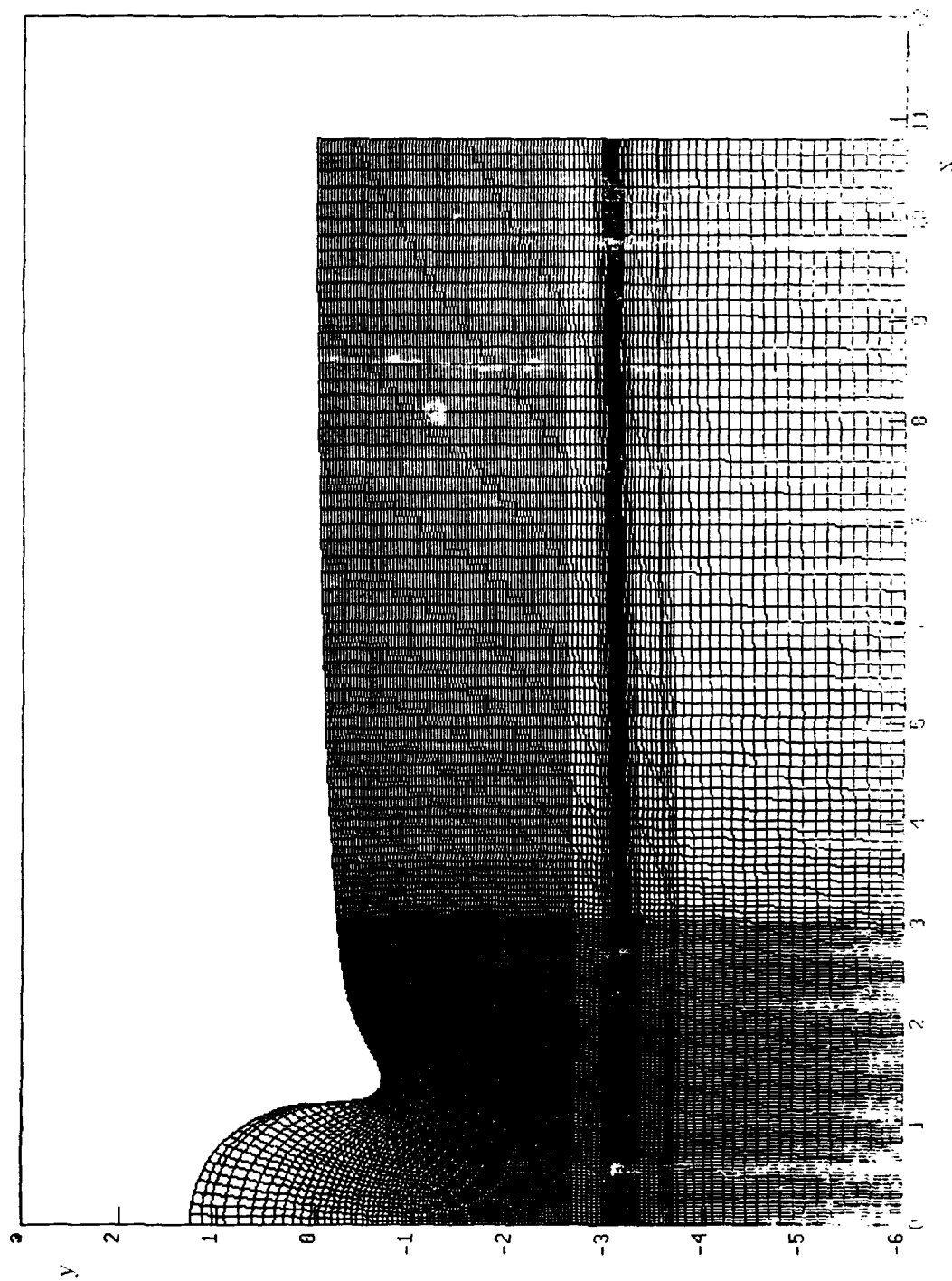
Fig. 3. Grid of the computational half-plane for $Re = 50$, $Fr = 1.125$, $t = 4.0$.
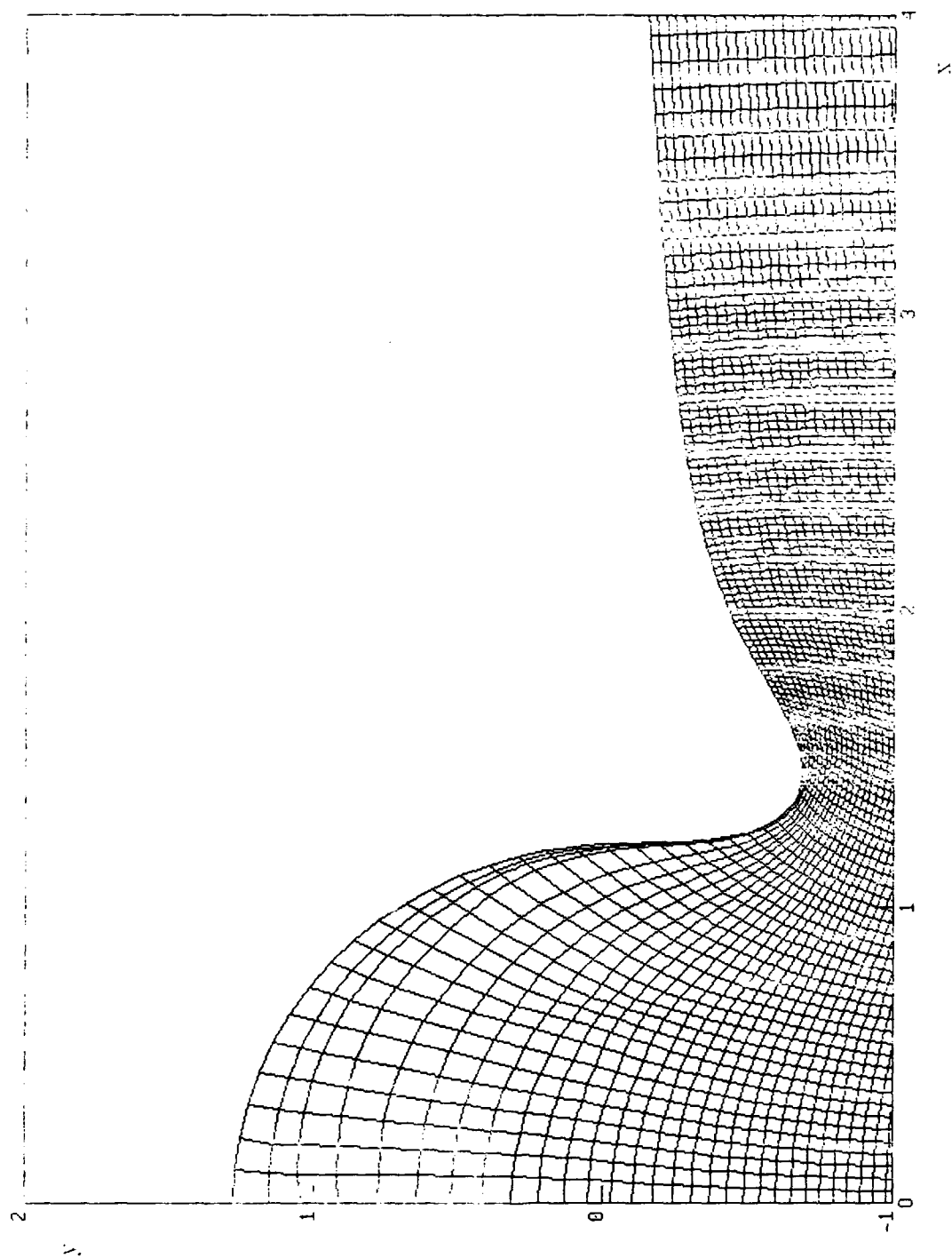
Fig. 4. Section of the grid displayed in Fig. 3.
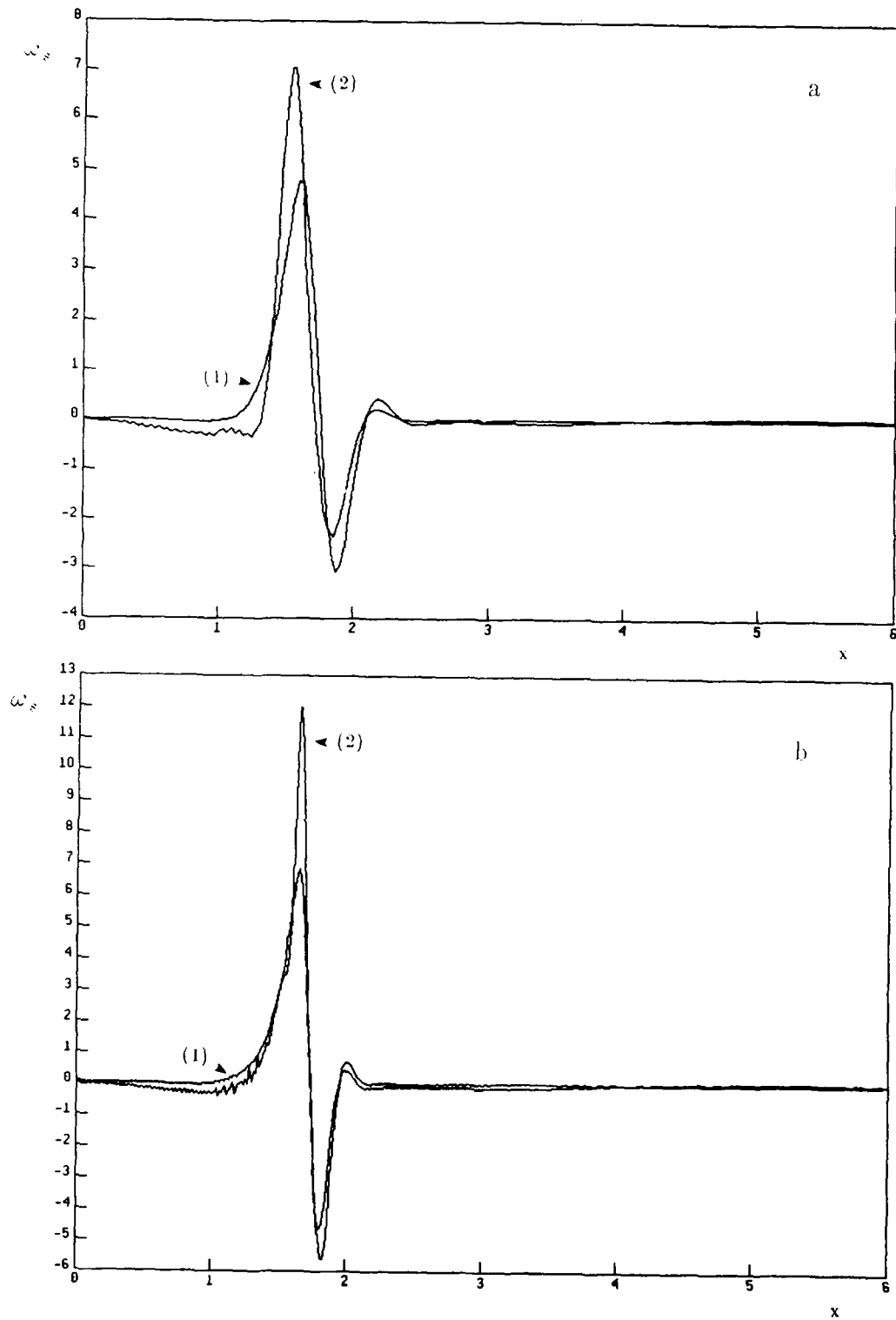
Fig. 5. Free-surface vorticity for $Re = 50$, $Fr = 0.356$, $t = 5.02$. (1) Computed with the velocity components according to $\omega = \partial v / \partial x - \partial u / \partial y$, and (2) computed with formula (58) for (a) the grid (157×135) and (b) the grid (313×269).

26
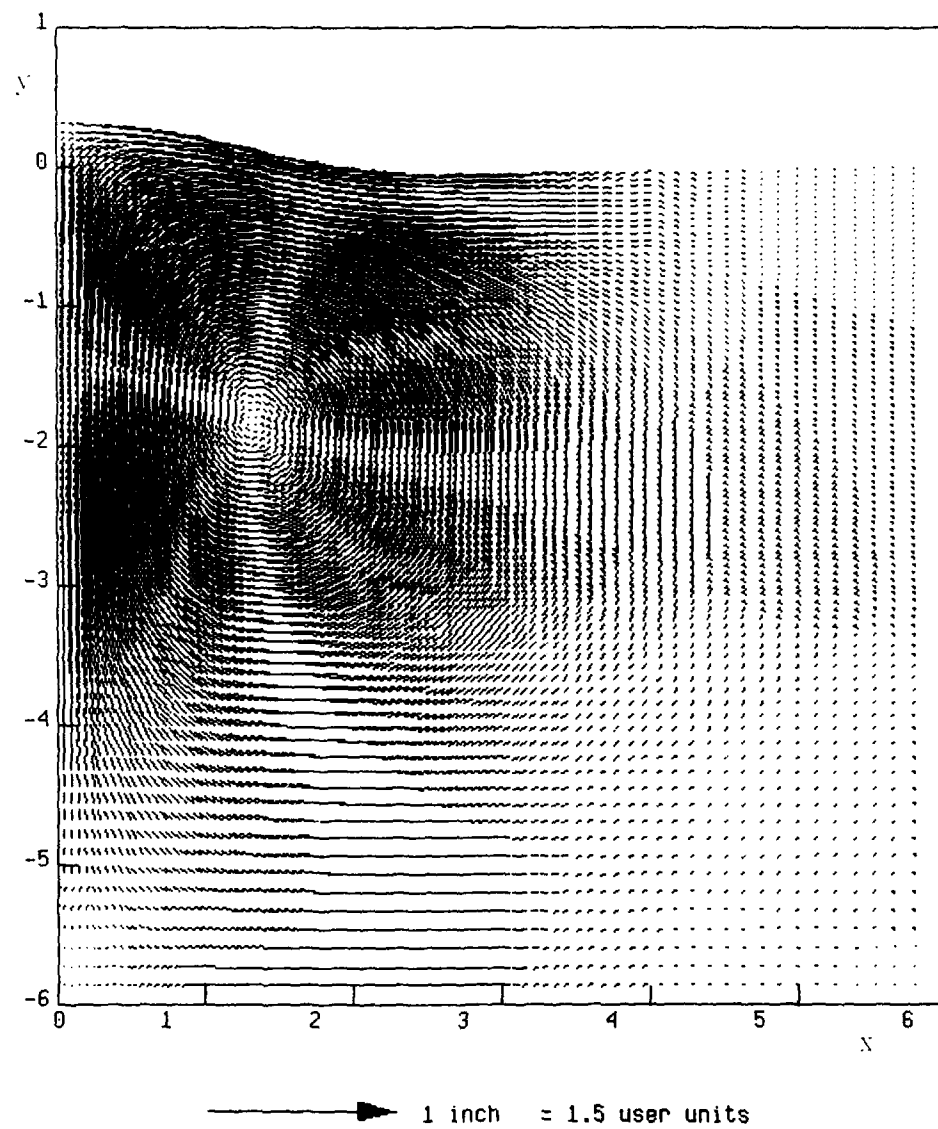
Fig. 6. Vector field of the velocity for $Re = 10$, $Fr = 1.125$ at $t = 4.0$.

27
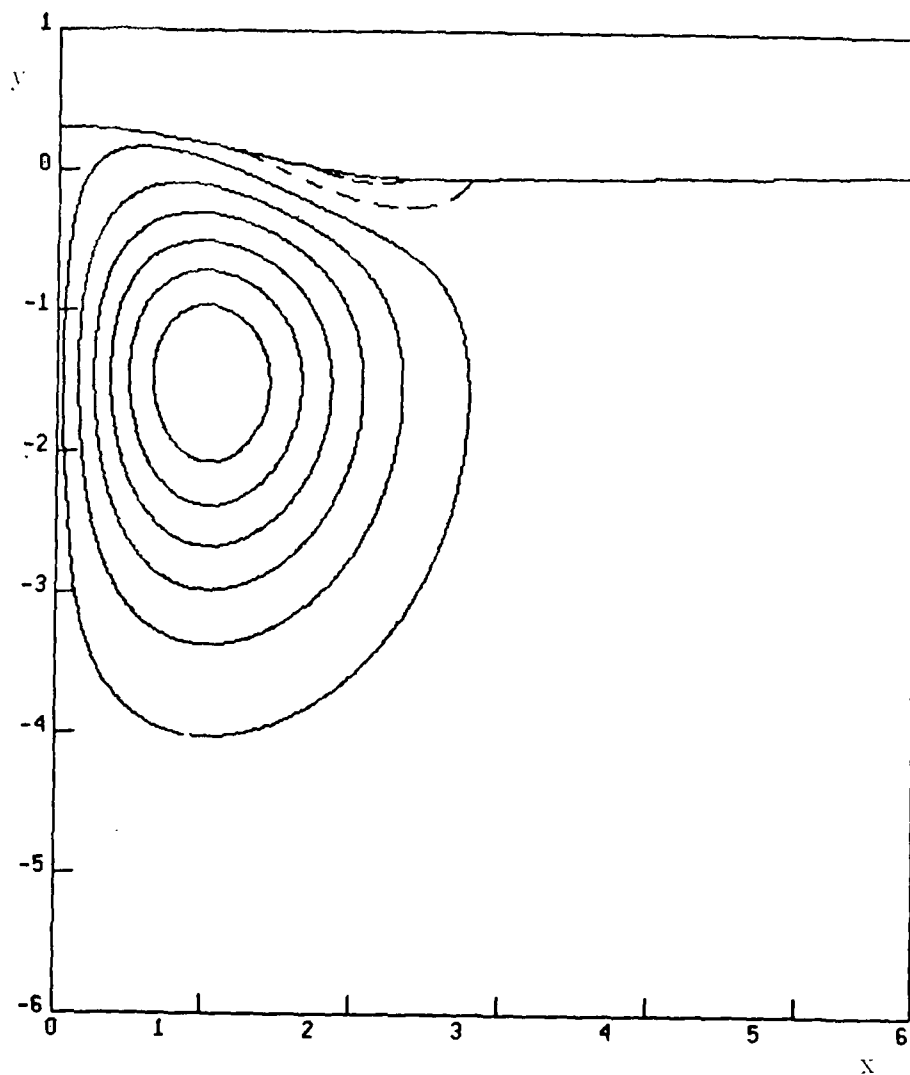
Fig. 7. Equi-vorticity lines for Re = 10, Fr = 1.125 at t = 4.48. The values of the contours are ±0.05, ±0.15, ±0.25, etc. Solid lines represent negative, dashed lines positive data.
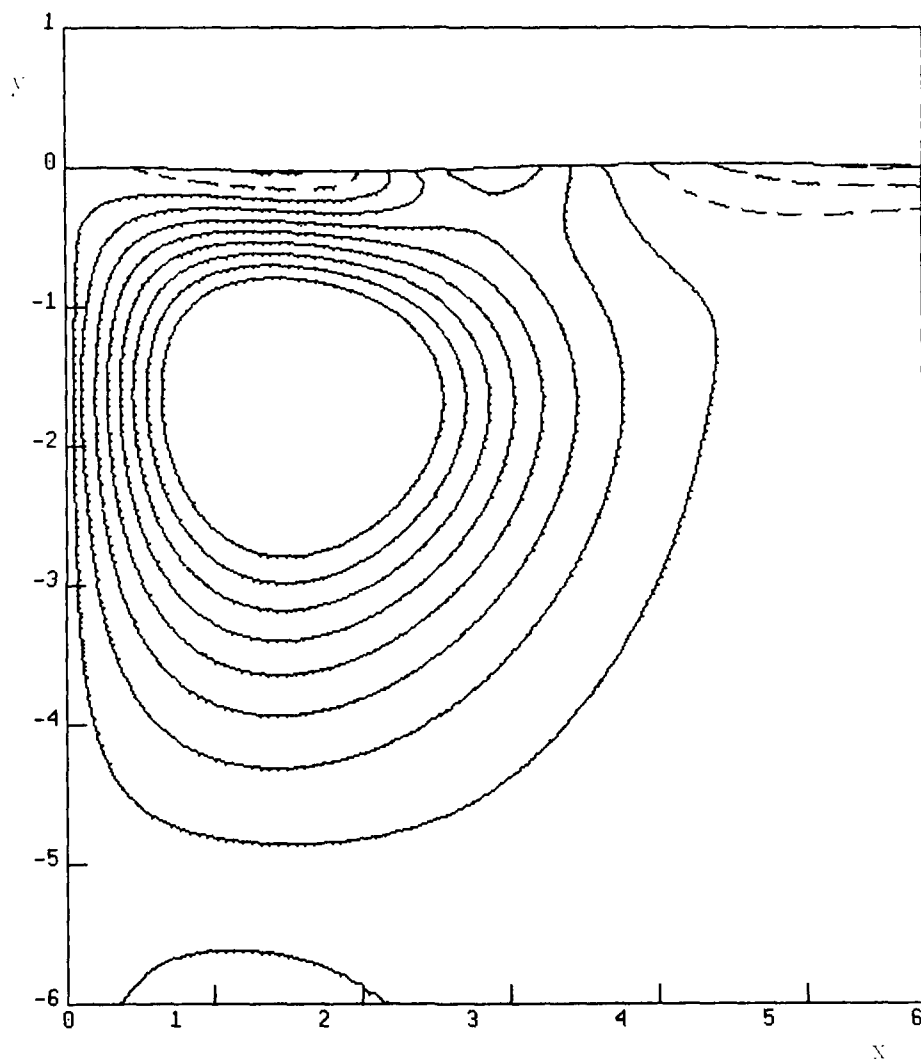
Fig. 8. Equi-vorticity lines for Re = 10, Fr = 1.125 at t = 9.04. The values of the contours are —0.15, —0.13, etc. Solid lines represent negative, dashed lines positive data.
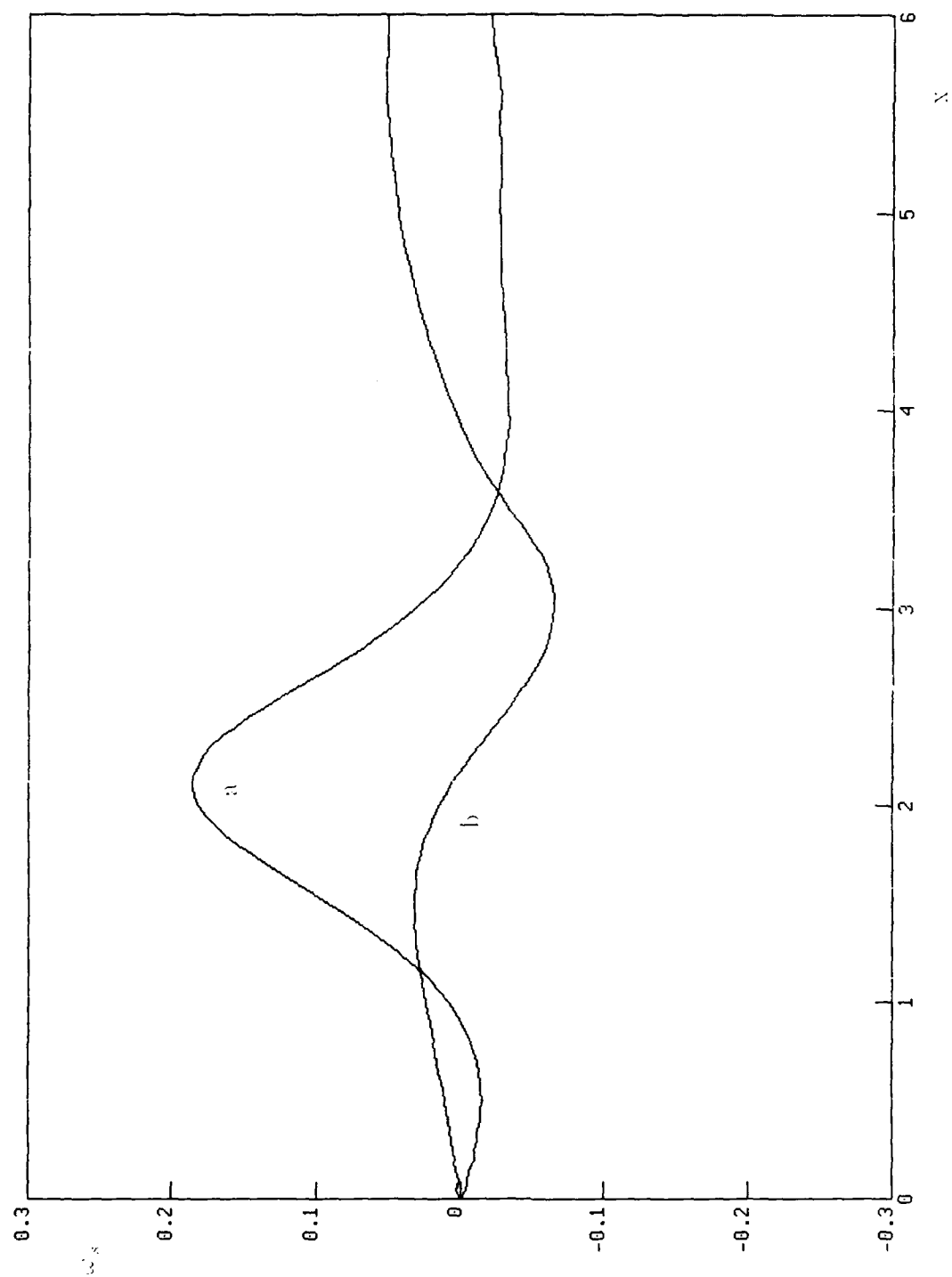
Fig. 9. Free-surface vorticity for Re = 10, Fr = 1.125 at (a) t = 4.48 and (b) t = 9.04.

30
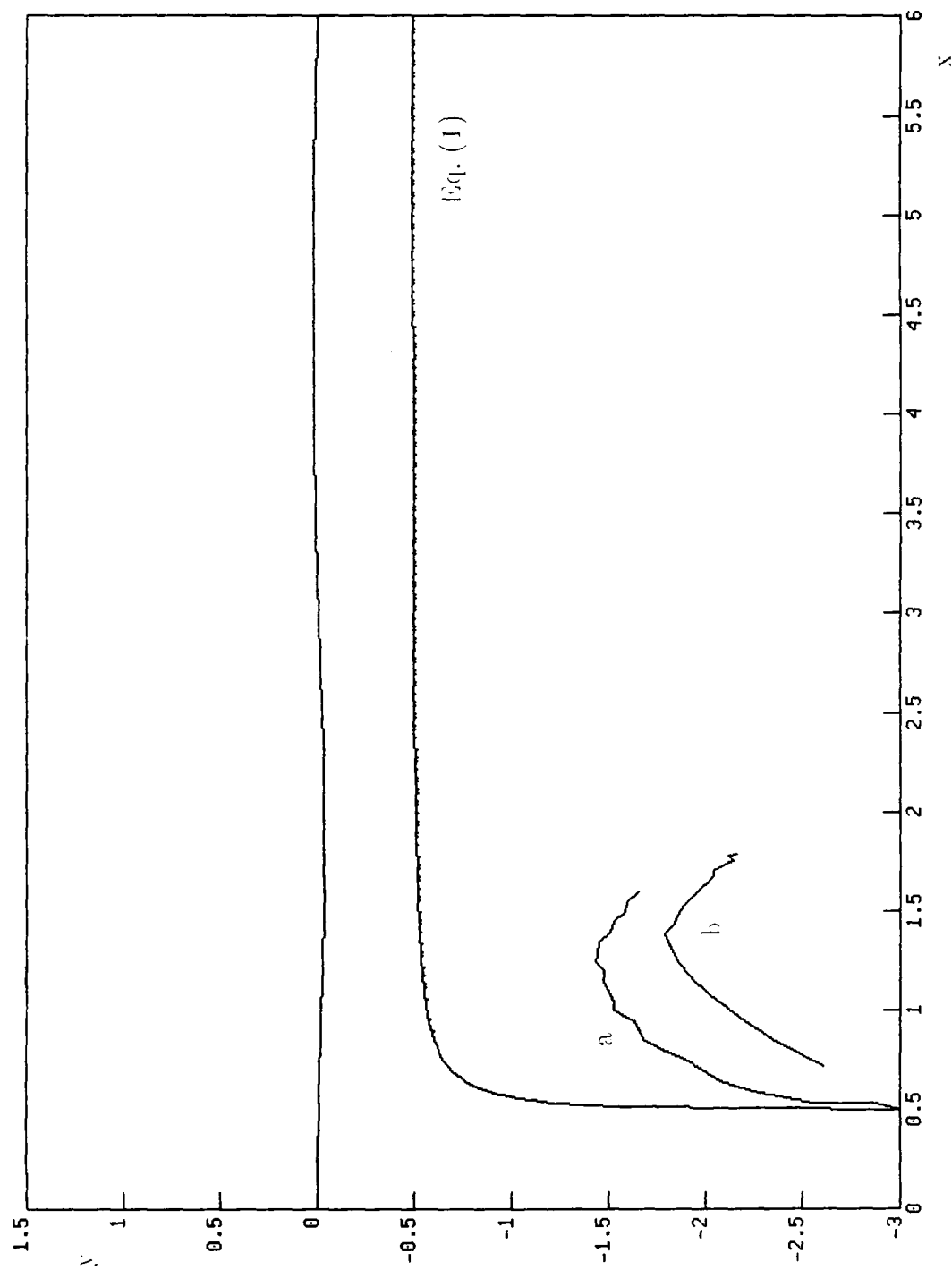
Fig. 10. Path of the vortex center for $Re = 10$, $Fr = 1.125$, defined (a) by $|z_{\min}|$, (b) by the center of the whirl. For comparison, Lamb's solution, Eq. (1), is added.

Fig. 11. Decrease of $|\omega_{min}|$ with time for Re = 10, $Fr = 1.125$.

32
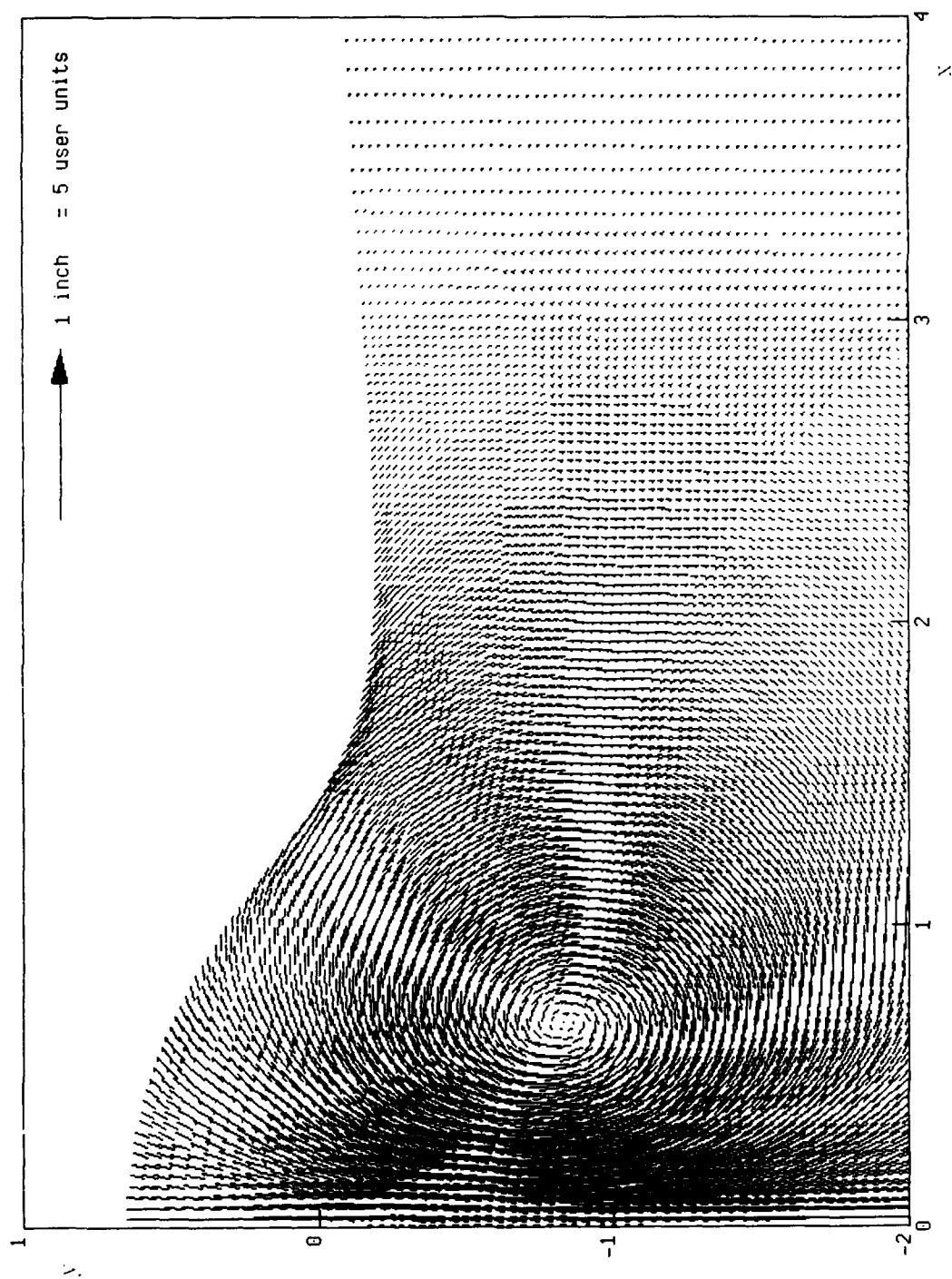
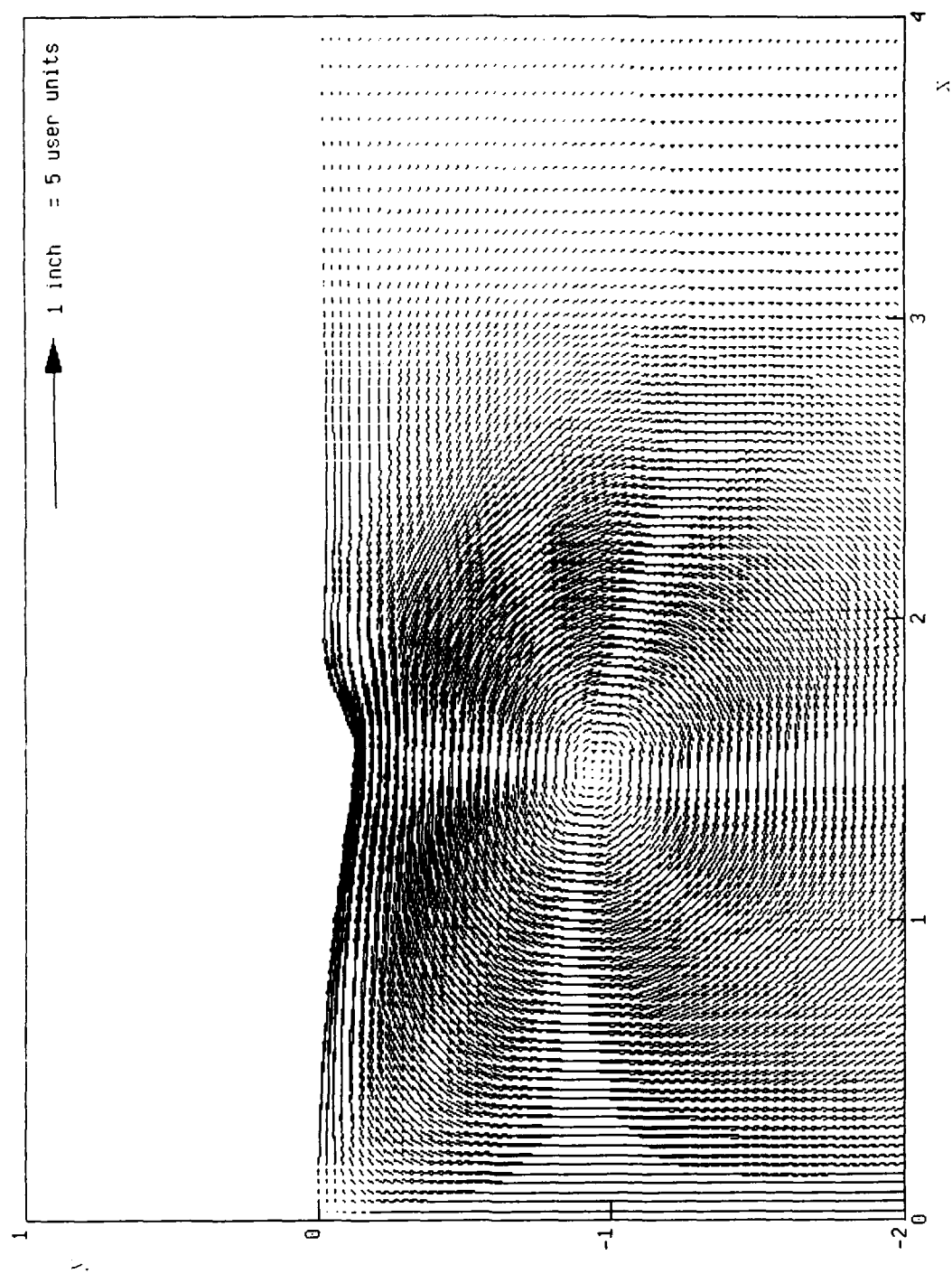Fig. 12. Vector field of the velocity for $Re = 50$, $Fr = 1.125$ at $t = 2.50$.
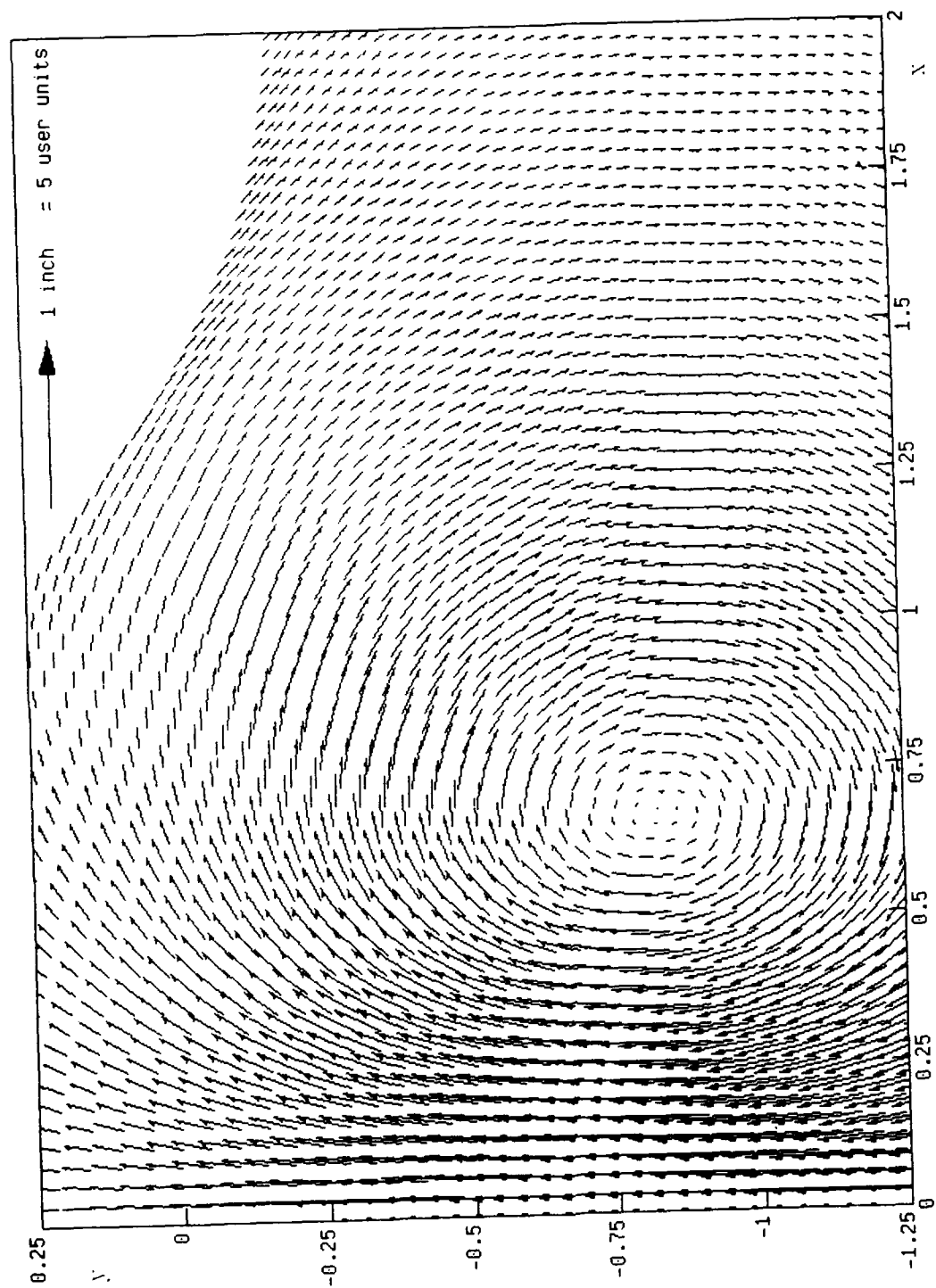
Fig. 13. Section of the flow field displayed in Fig. 12.

34
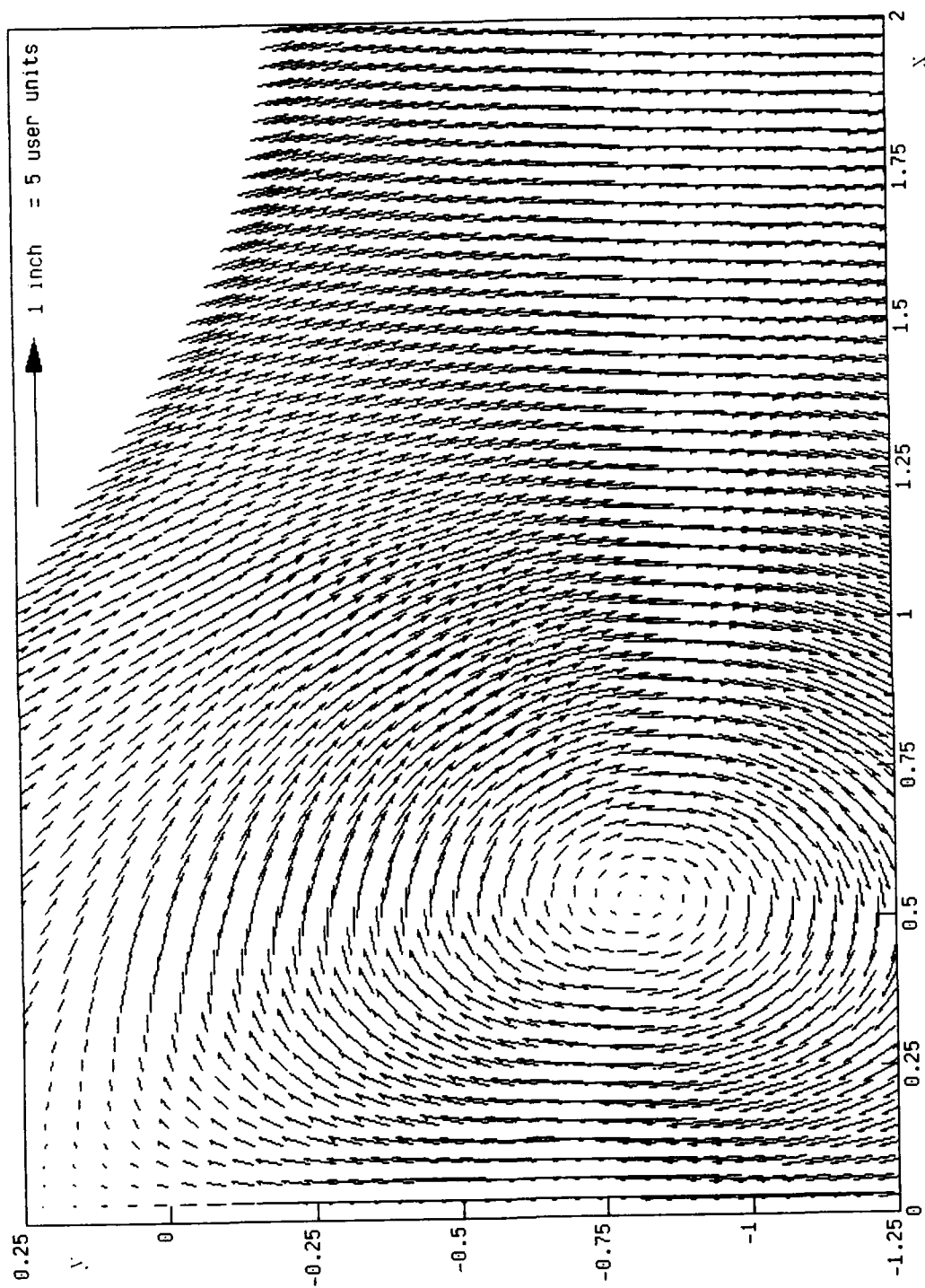
Fig. 14. Same flow field as in Fig. 13 but with reference frame fixed to the vortex center.

35
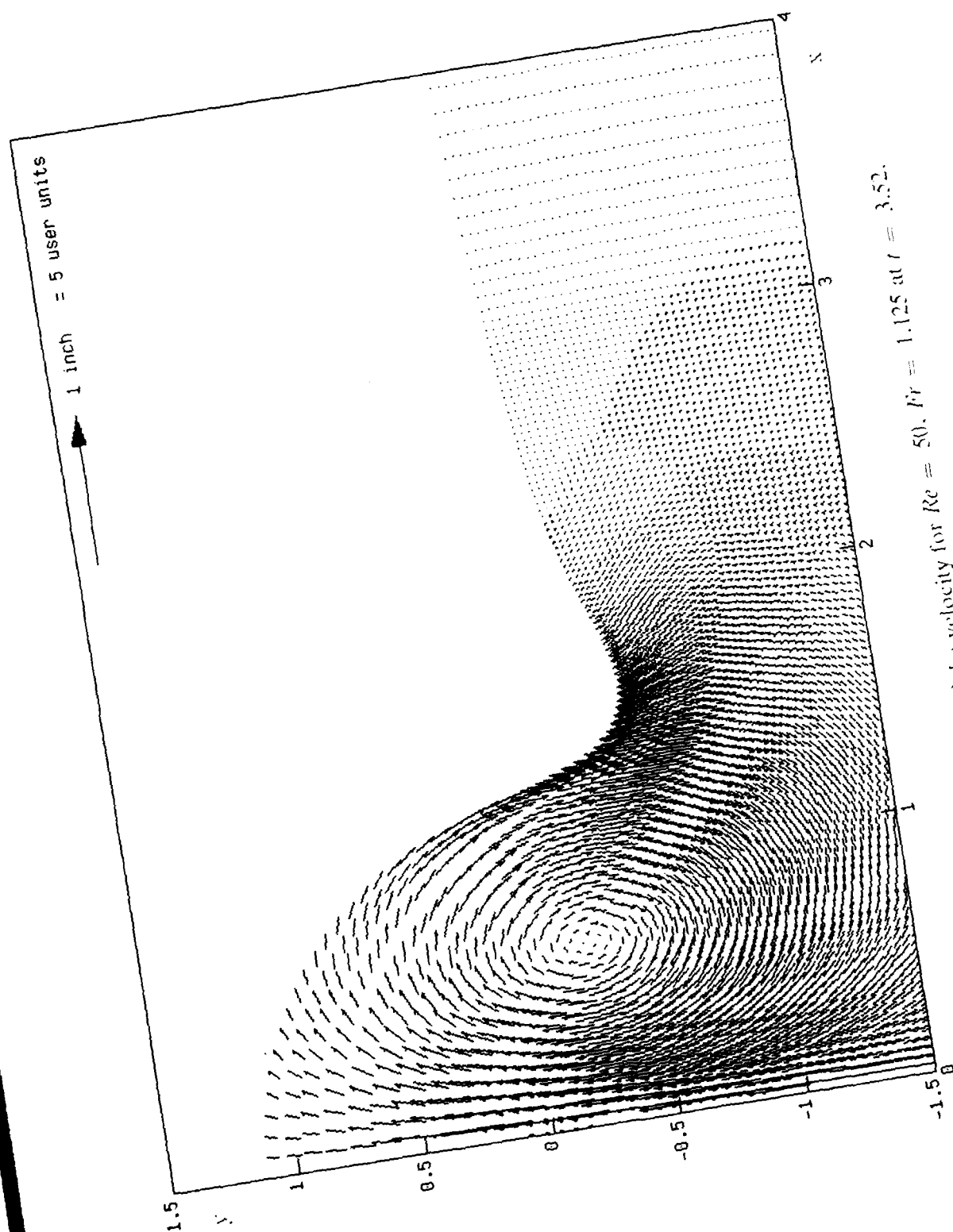
Fig. 15. Vector field of the velocity for $Re = 50$, $Pr = 1.125$ at $t = 3.52$.

36

1 inch = 5 user units
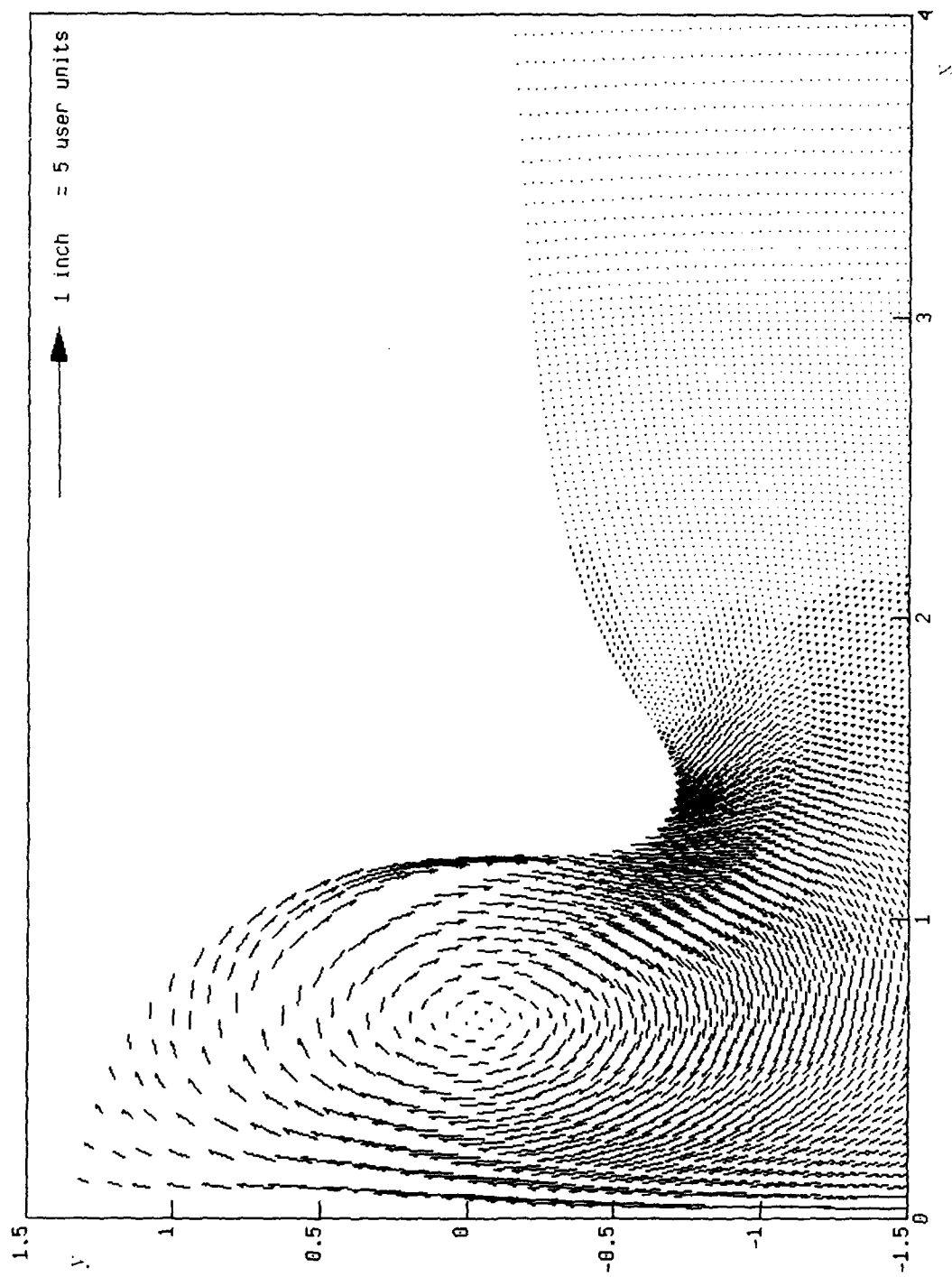
Fig. 16. Vector field of the velocity for $Re = 50$, $Pr = 1.125$ at $t = 4.06$.
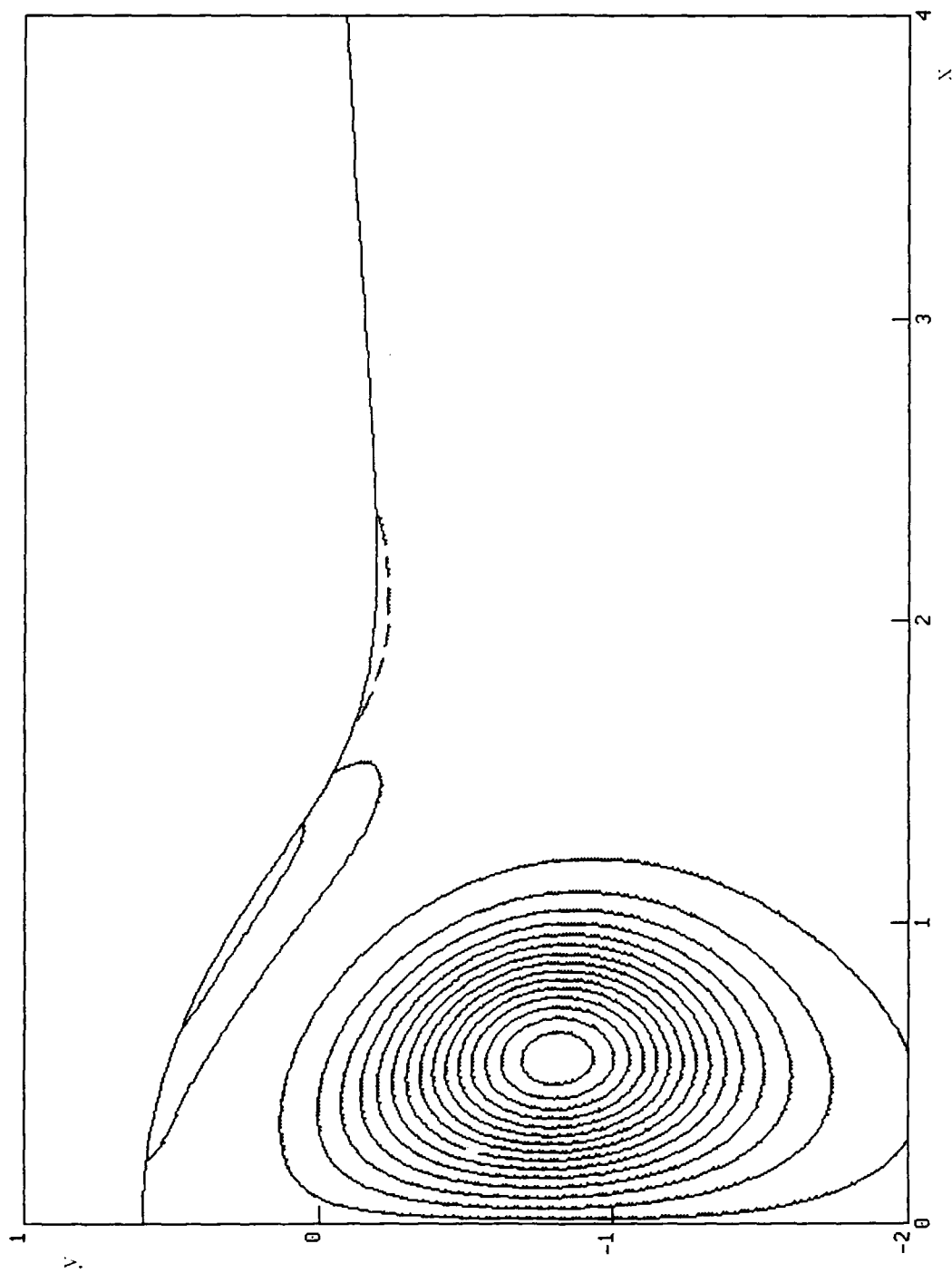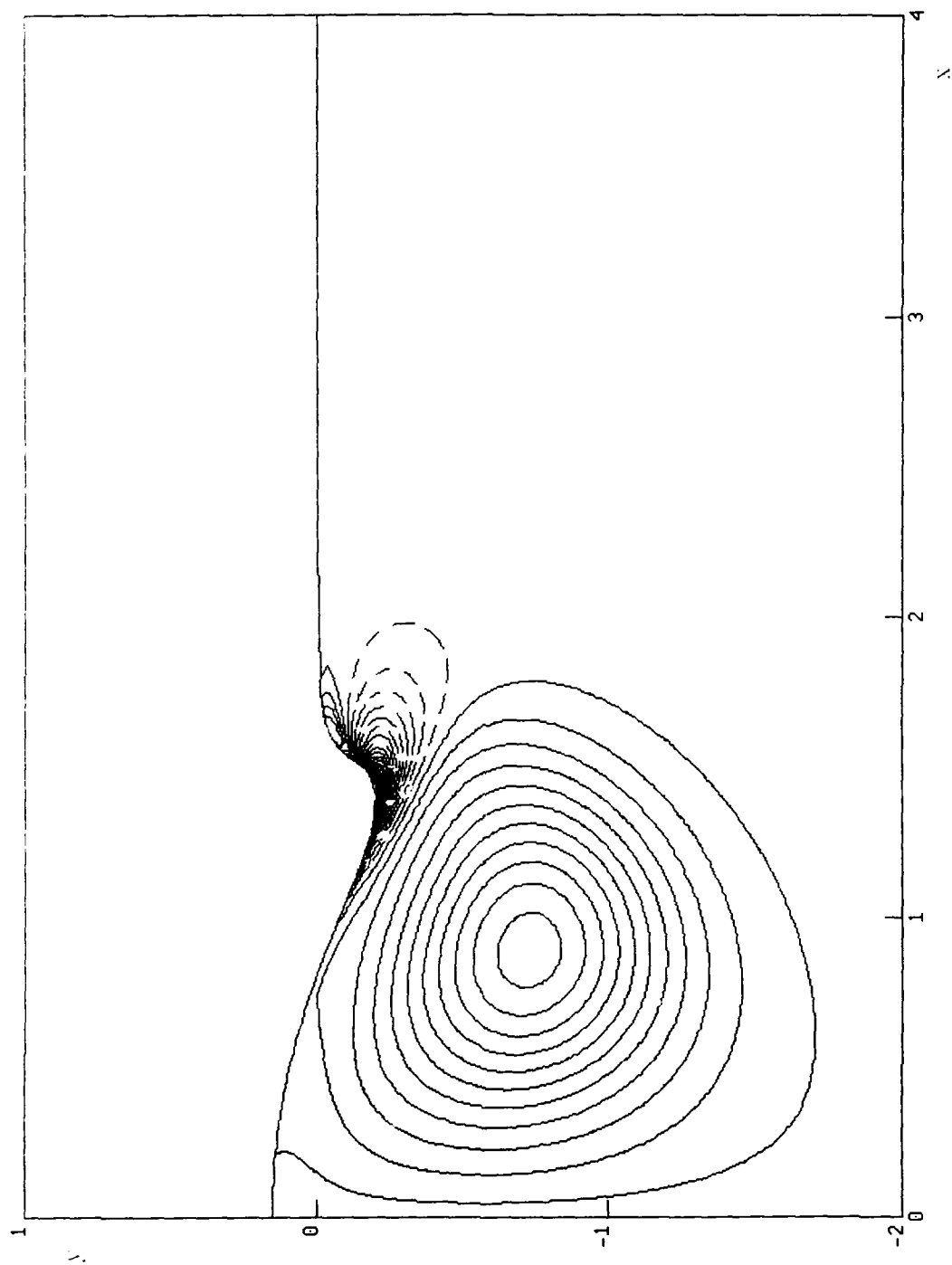
Fig. 17. Equi-vorticity lines for $Re = 50$, $Pr = 1.125$ at $t = 2.50$. The values of the contours are ± 0.3, ± 0.9, ± 1.5, etc. Solid lines represent negative, dashed lines positive data.

38
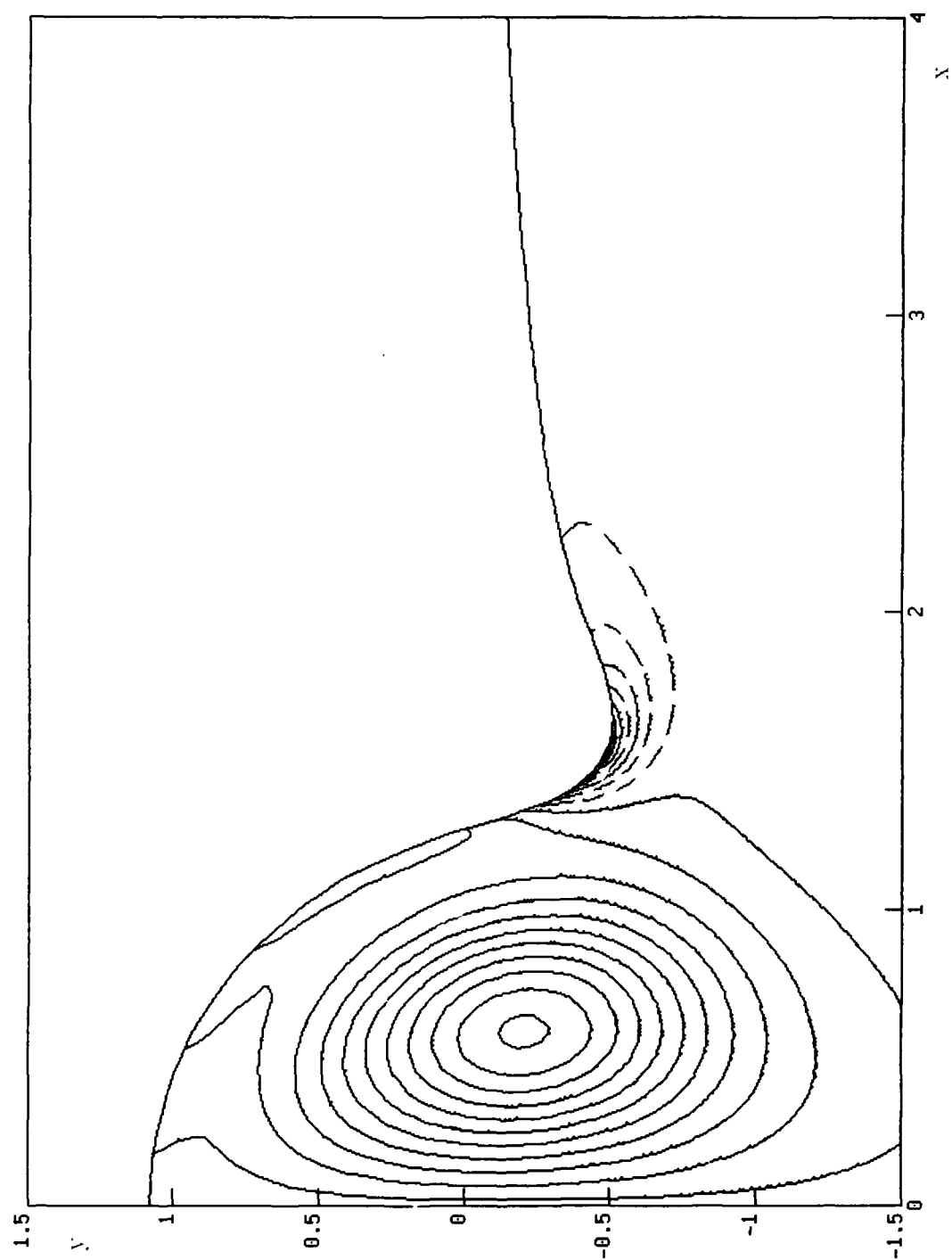
Fig. 18. Equi-vorticity lines for $Re = 50$, $Fr = 1.125$ at $t = 3.52$. The values of the contours are ± 0.3, ± 0.9, ± 1.5, etc. Solid lines represent negative, dashed lines positive data.
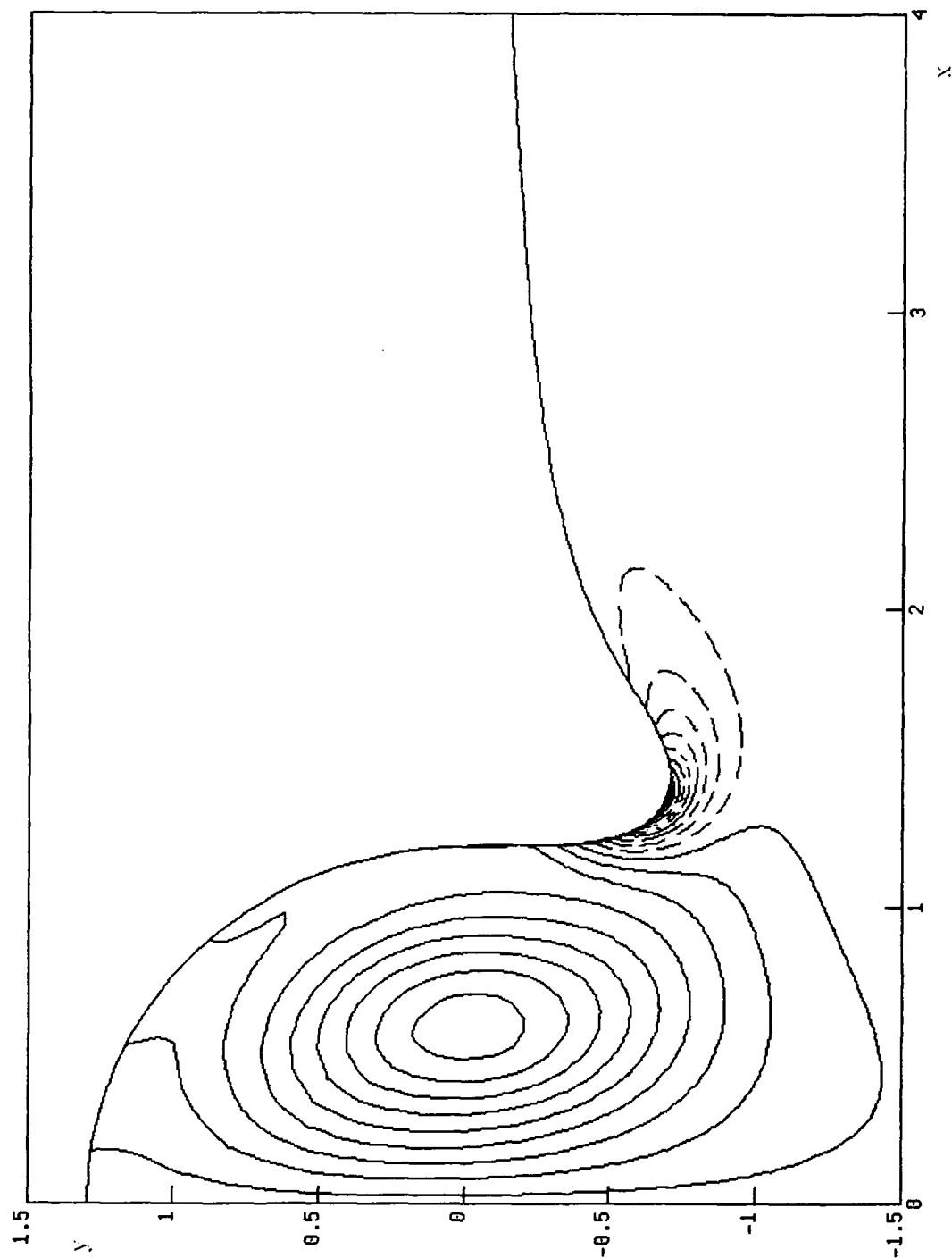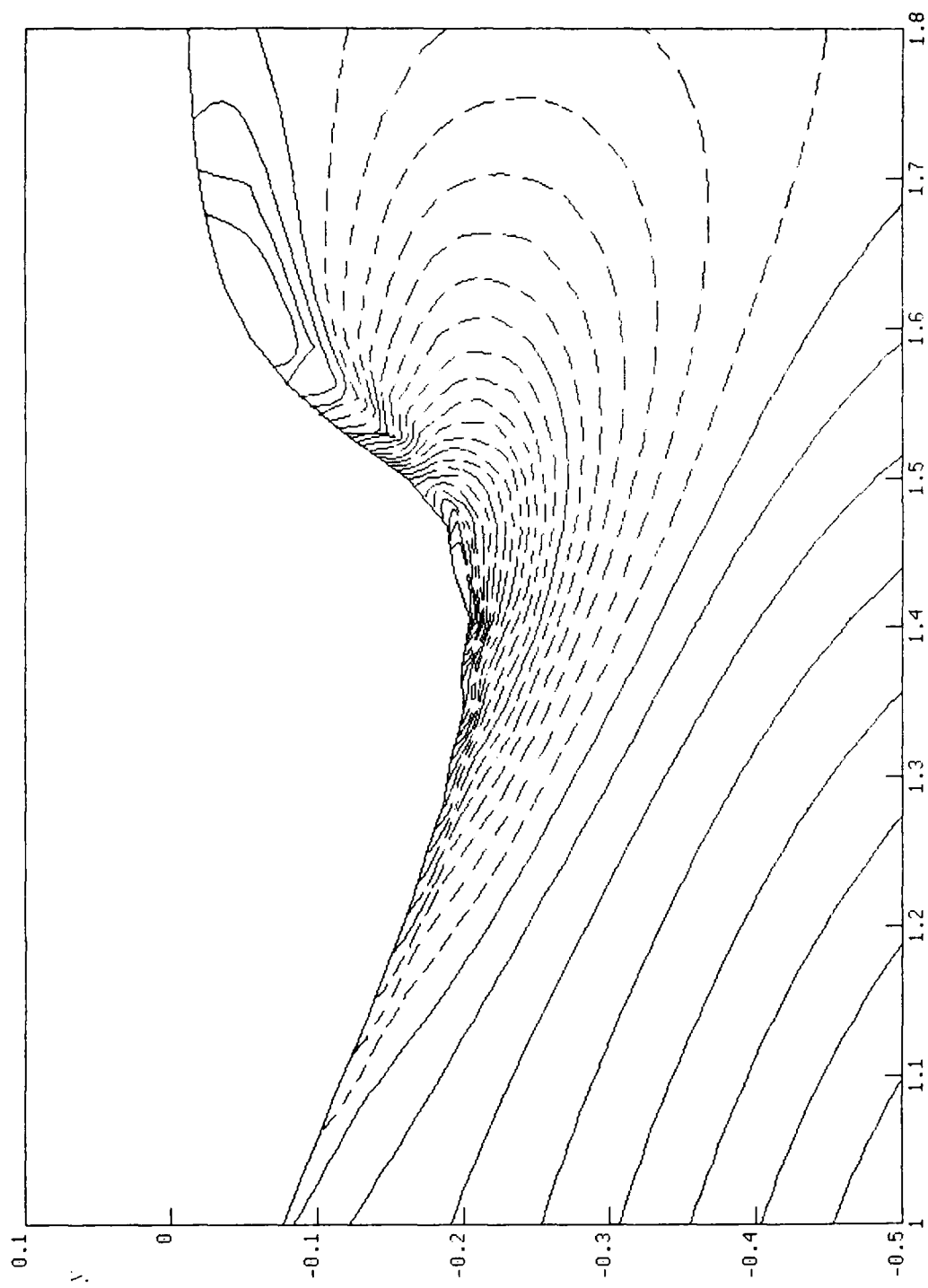
Fig. 19. Equi-vorticity lines for $Re = 50$, $Fr = 1.125$ at $t = 4.06$. The values of the contours are ± 0.3, ± 0.9, ± 1.5, etc. Solid lines represent negative, dashed lines positive data.
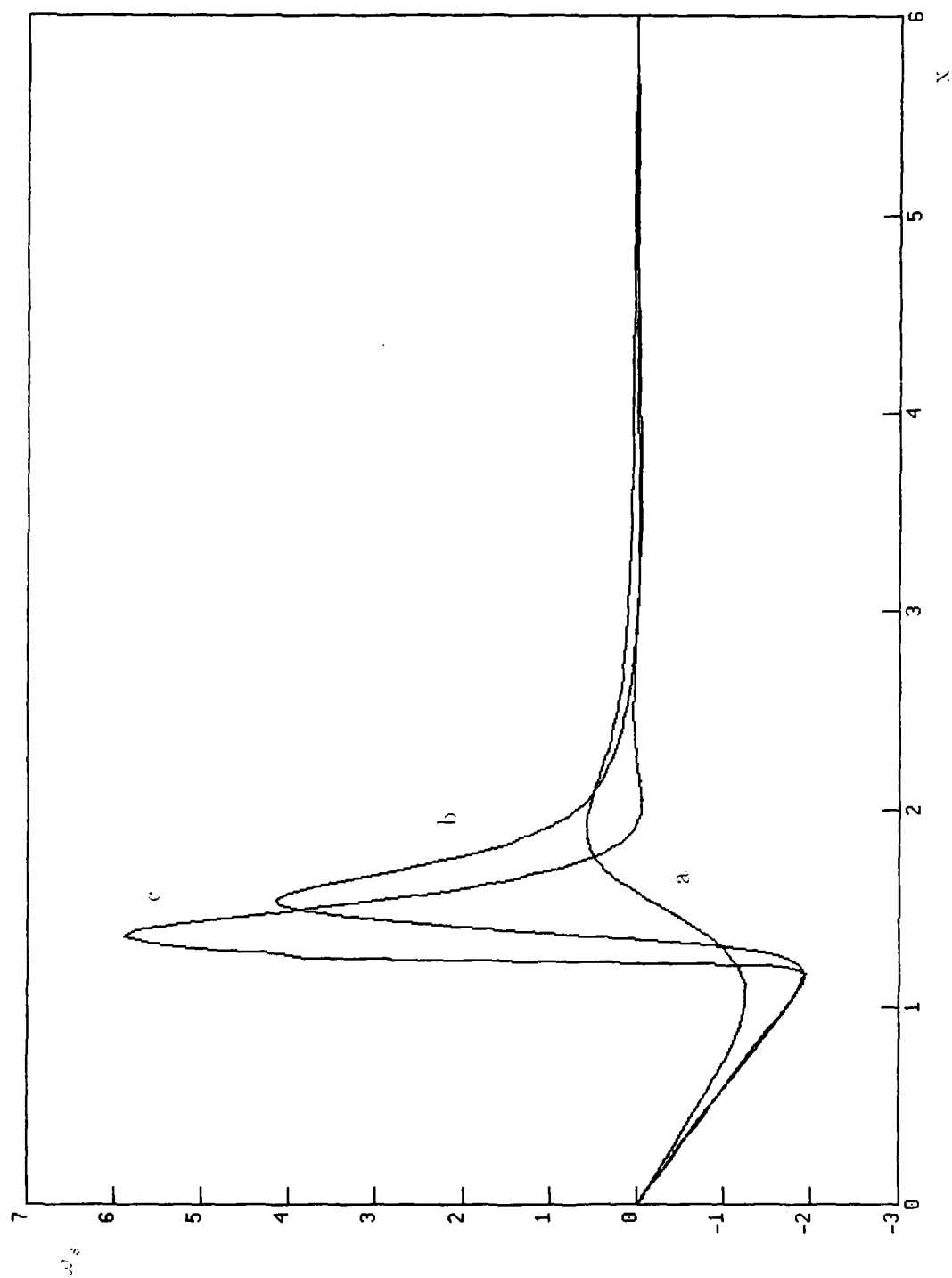
Fig. 20. Free-surface vorticity for $Re = 50$, $Fr = 1.125$ at (a) $t = 2.50$, (b) $t = 3.52$, and (c) $t = 4.00$.
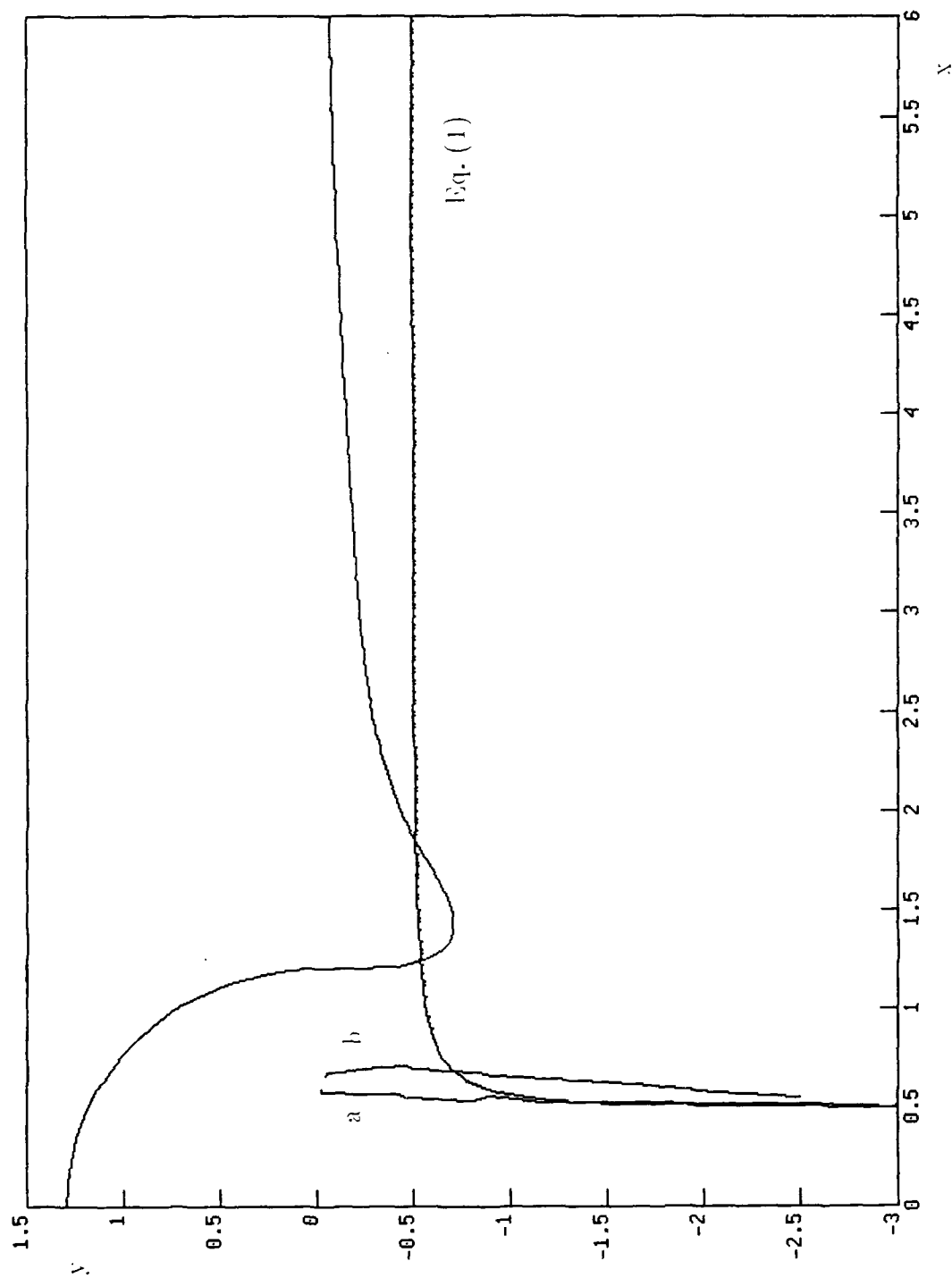
Fig. 21. Path of the vortex center for $Re = 50$, $Fr = 1.125$, defined (a) by $|\omega_{min}|$, (b) by the center of the whirl. For comparison, Lamb's solution, Eq. (1), is added. Also, the free surface at the last computed time $t = 4.06$ is presented.

42
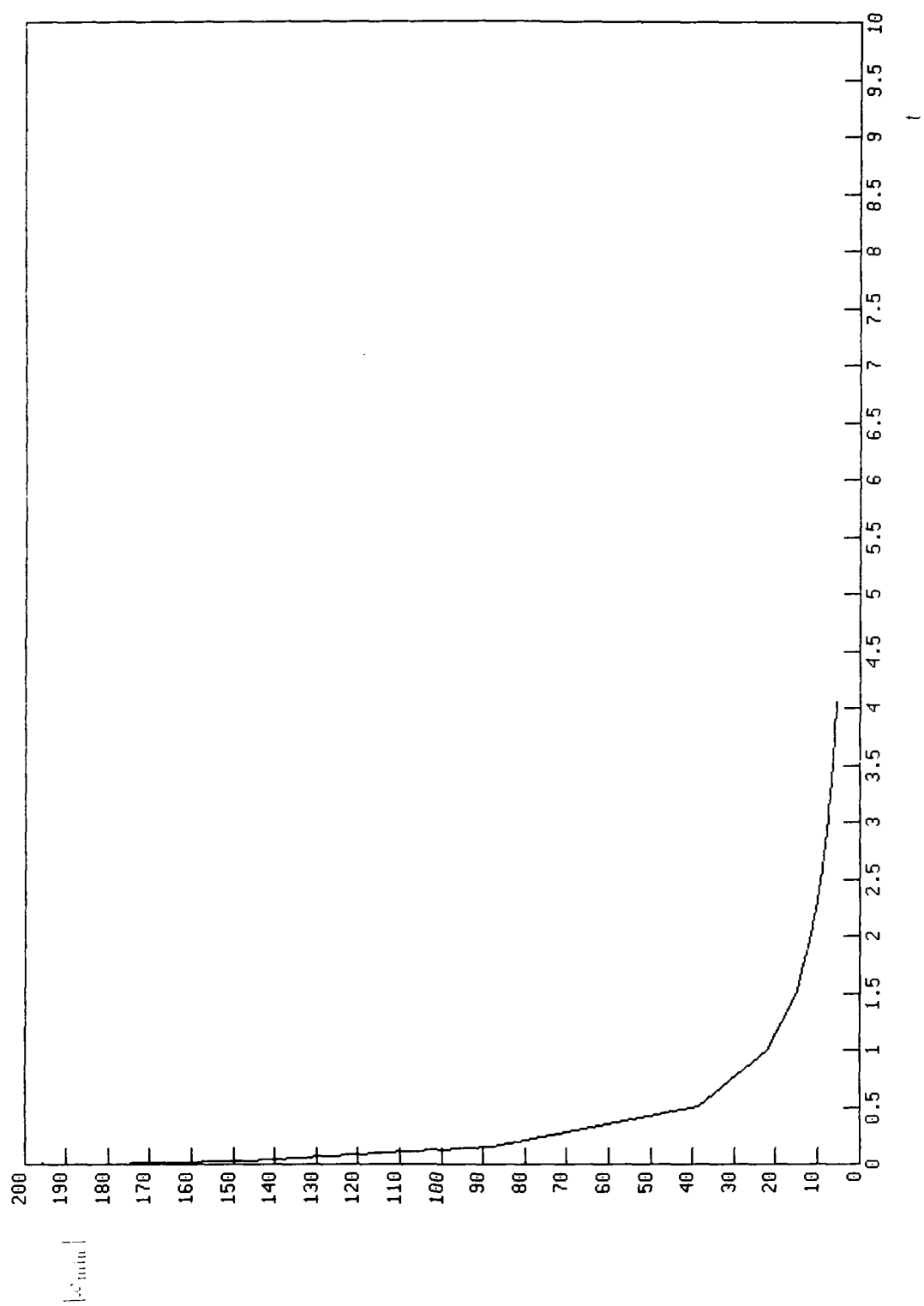
Fig. 22. Decrease of $|\psi_{\min}|$ with time for $Re = 50$, $Pr = 1.125$.

43
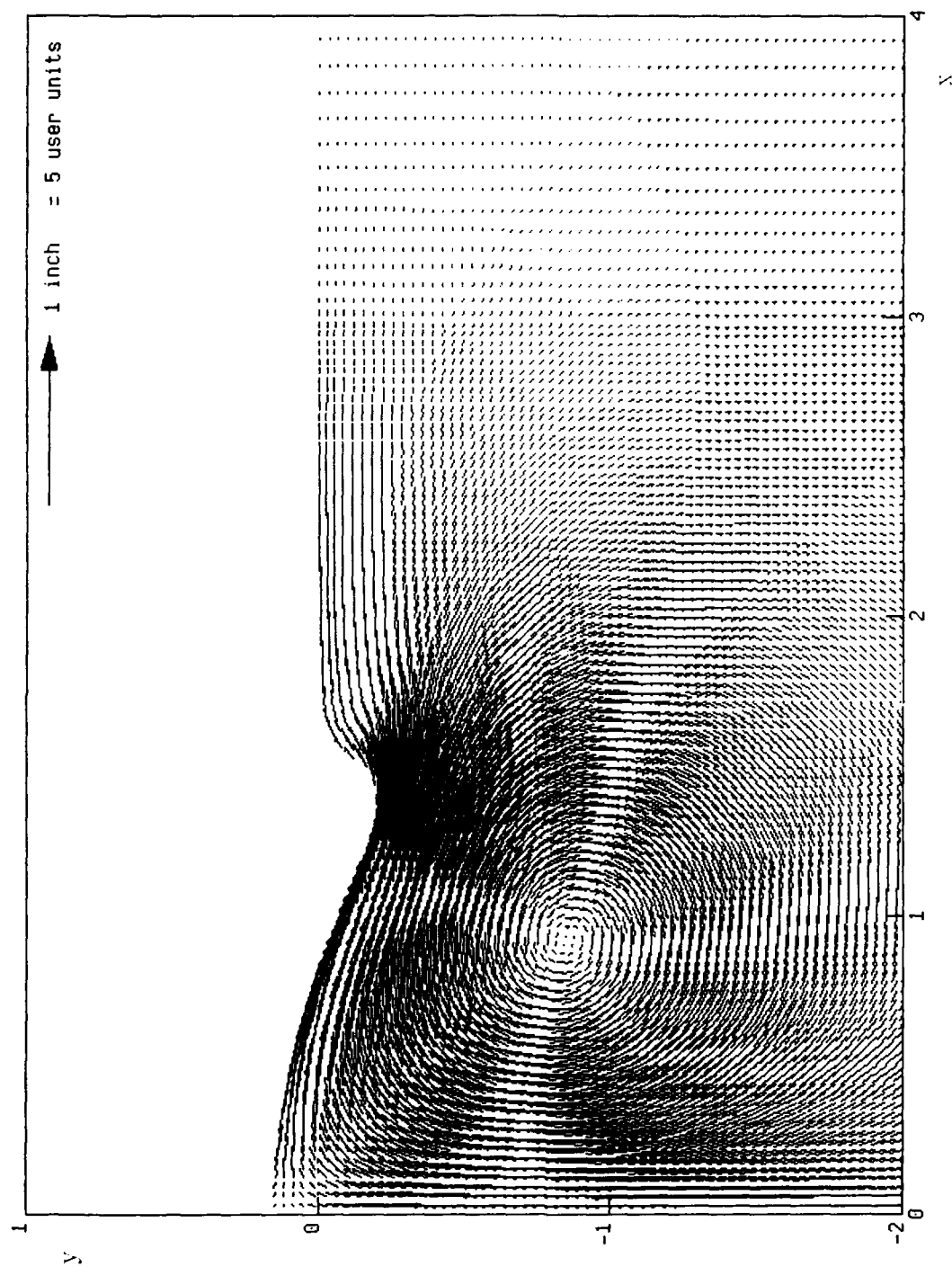
Fig. 23. Vector field of the velocity for $Re = 50$, $Fr = 0.356$ at $t = 3.52$.

Fig. 24. Vector field of the velocity for $Re = 50$, $Fr = 0.356$ at $t = 5.02$.

45
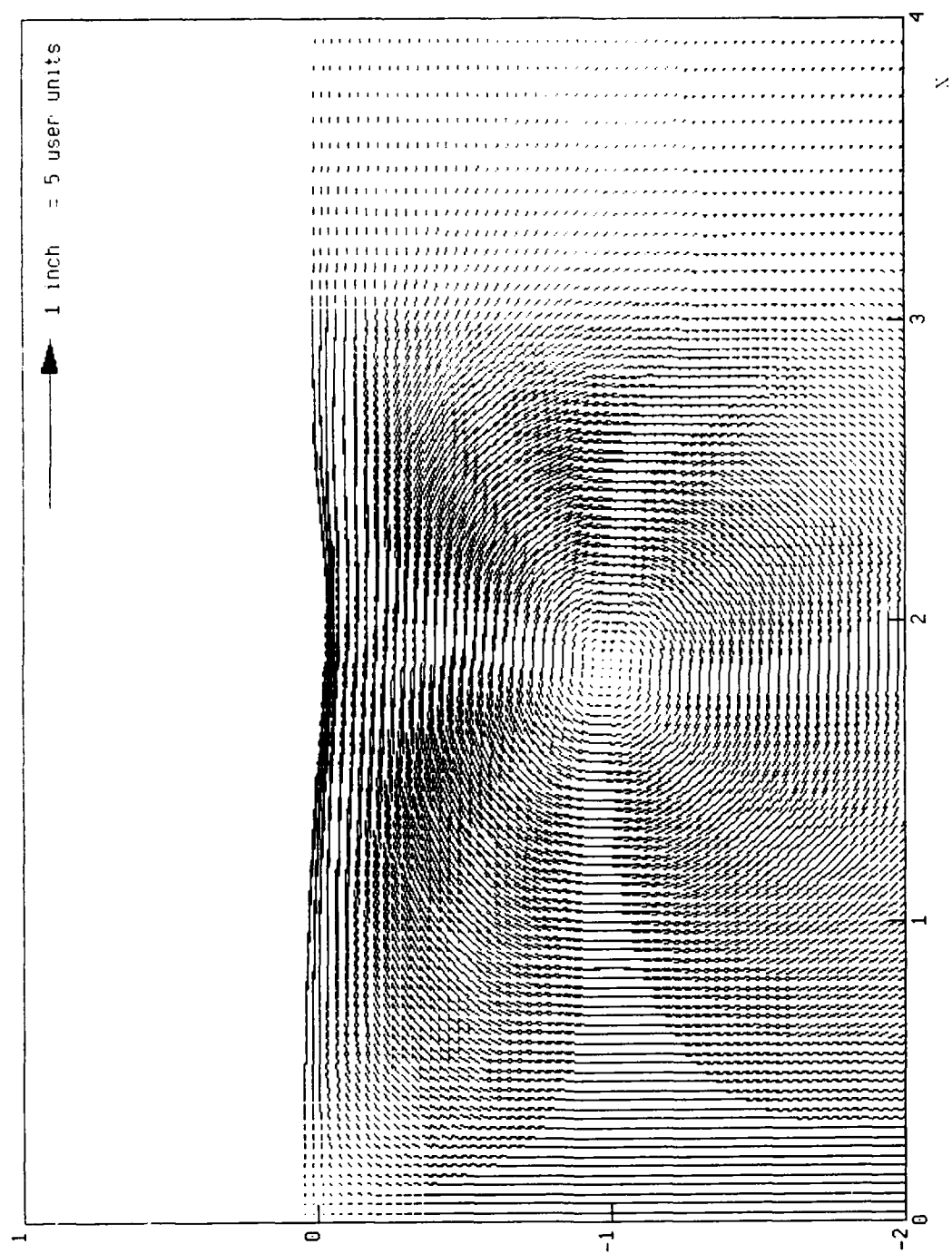
Fig. 25. Vector field of the velocity for $Re = 50$, $Fr = 0.356$ at $t = 6.52$.
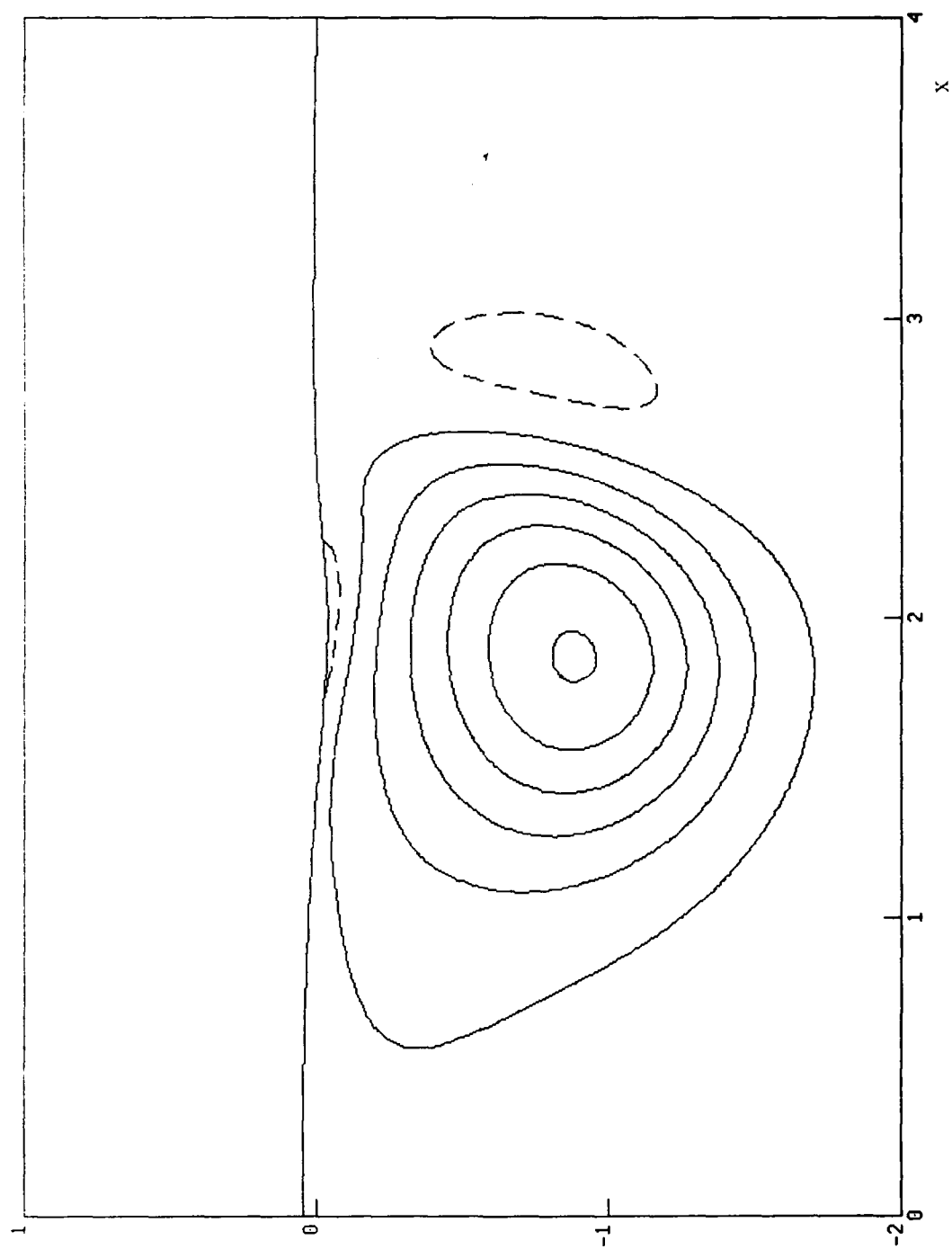
46

Fig. 26. Equi-vorticity lines for $Re \cdot 50$, $Pr = 0.356$ at $t = 3.52$. The values of the contours are ± 0.3, ± 0.9, ± 1.5, etc. Solid lines represent negative, dashed lines positive data.
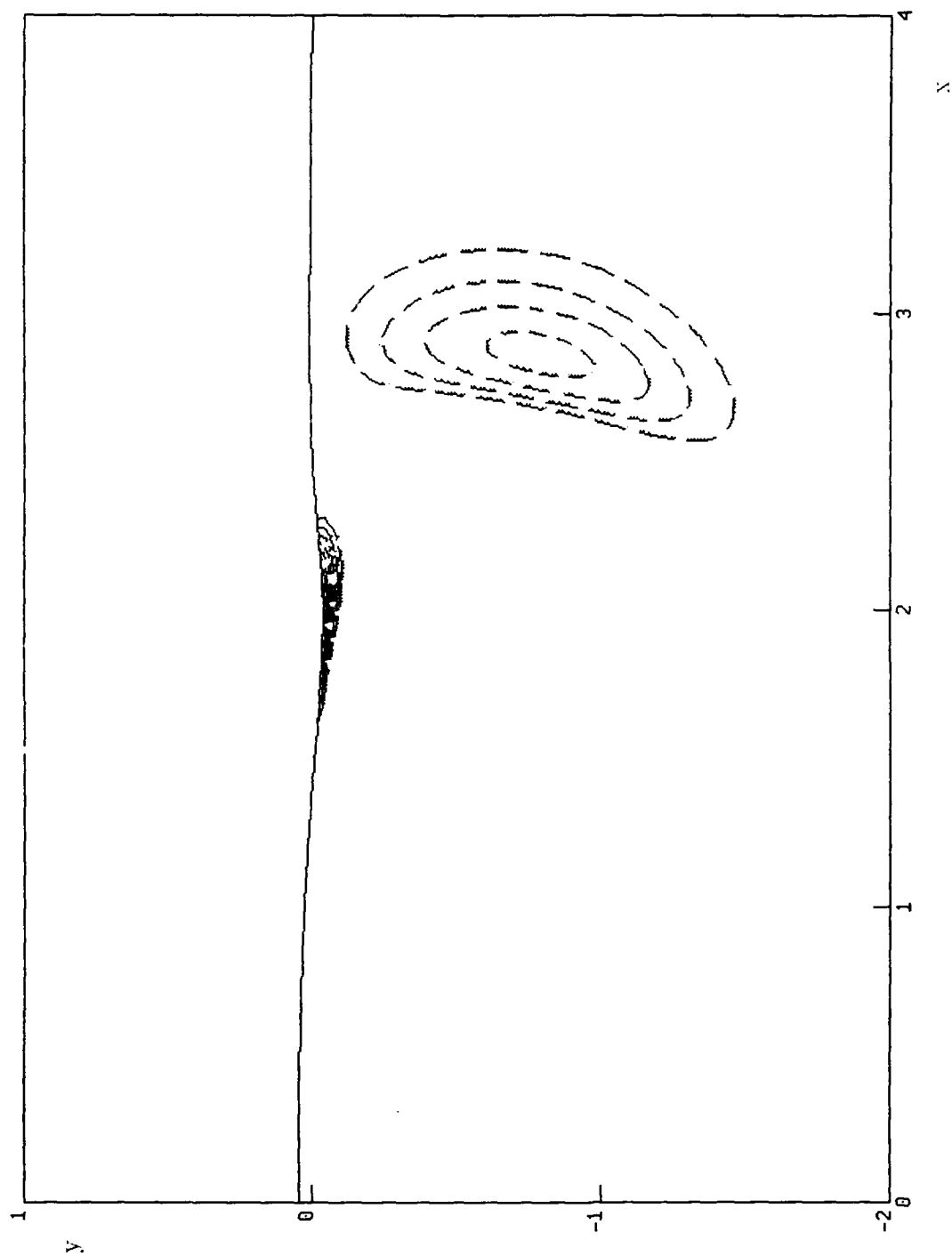
Fig. 27. Section of the vorticity field displayed in Fig. 26.
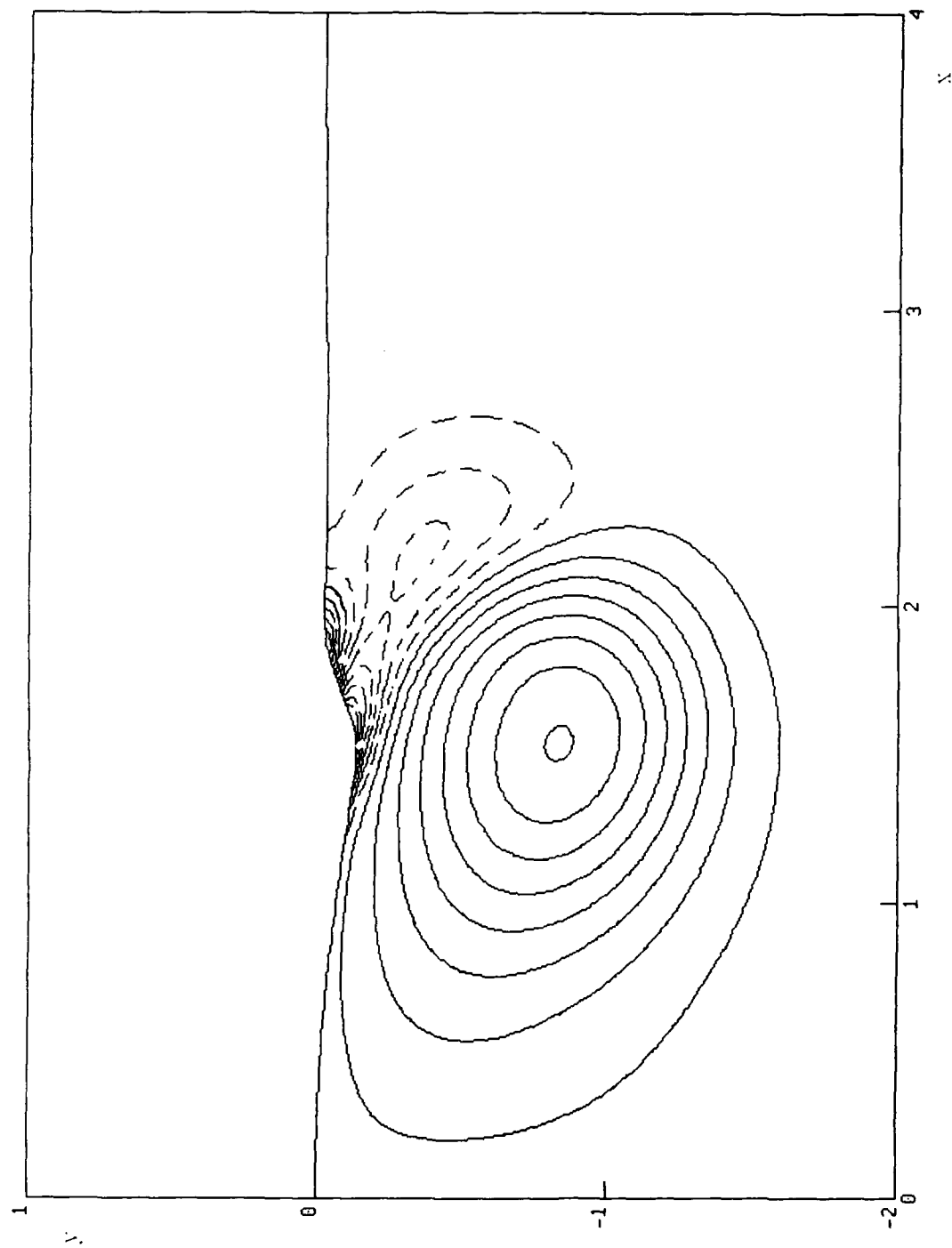
Fig. 28. Equi-vorticity lines for $Re = 50$, $Fr = 0.356$ at $t = 5.02$, grid size (157×135). The values of the contours are ± 0.3, ± 0.9, ± 1.5, etc. Solid lines represent negative, dashed lines positive data.
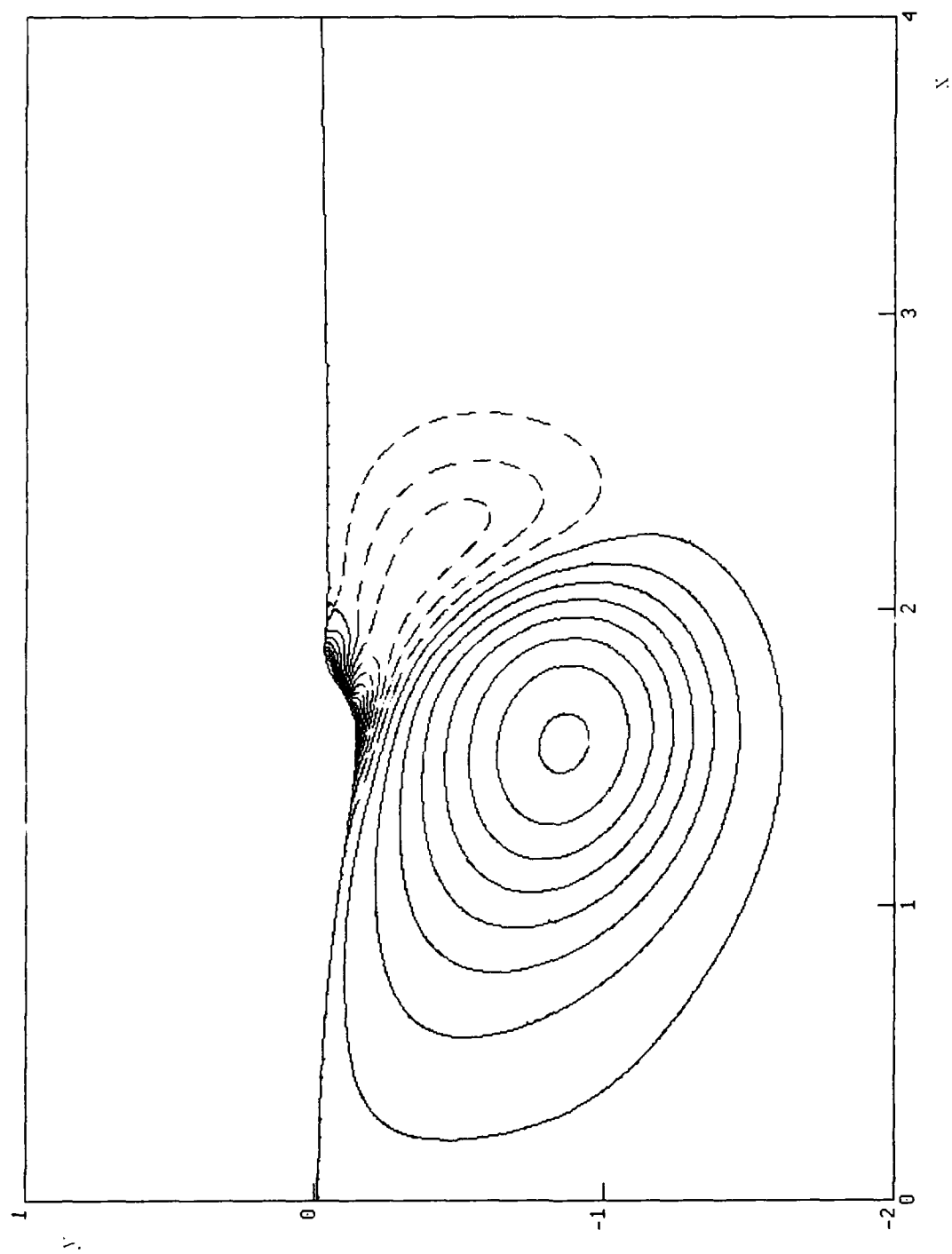
Fig. 29. Equi-vorticity lines for $Re = 50$, $Fr = 0.356$ at $t = 5.02$, grid size (313×269). The values of the contours are ± 0.3, ± 0.9, ± 1.5, etc. Solid lines represent negative, dashed lines positive data.

Fig. 30. Equi-vorticity lines for $Re = 50$, $Fr = 0.356$ at $t = 6.52$. The values of the contours are ± 0.3, ± 0.9, ± 1.5, etc. Solid lines represent negative, dashed lines positive data.

51

Fig. 31. Section of the vorticity field displayed in Fig. 30. The values of the contours are 0.1, 0.2, 0.3, etc.
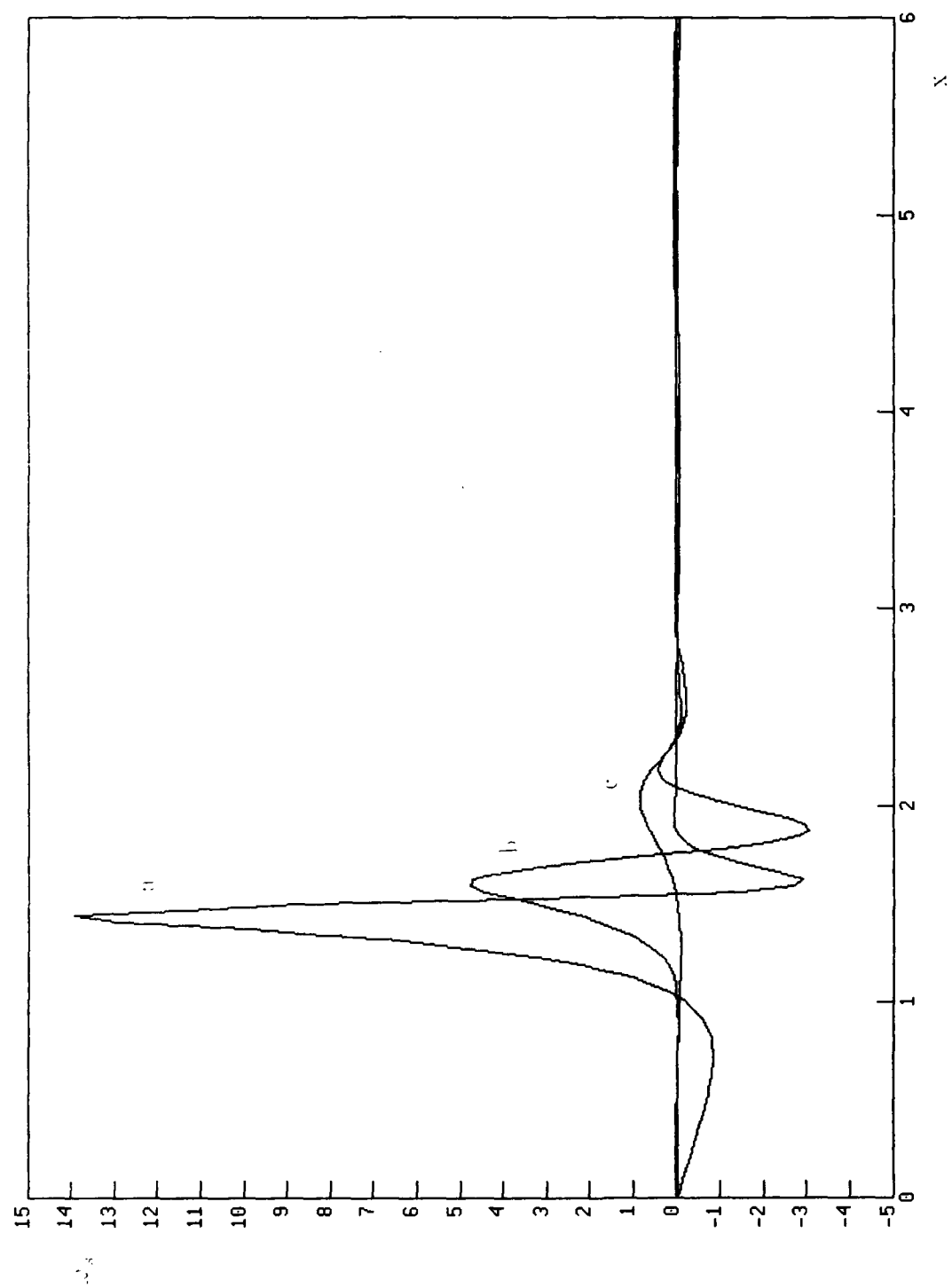
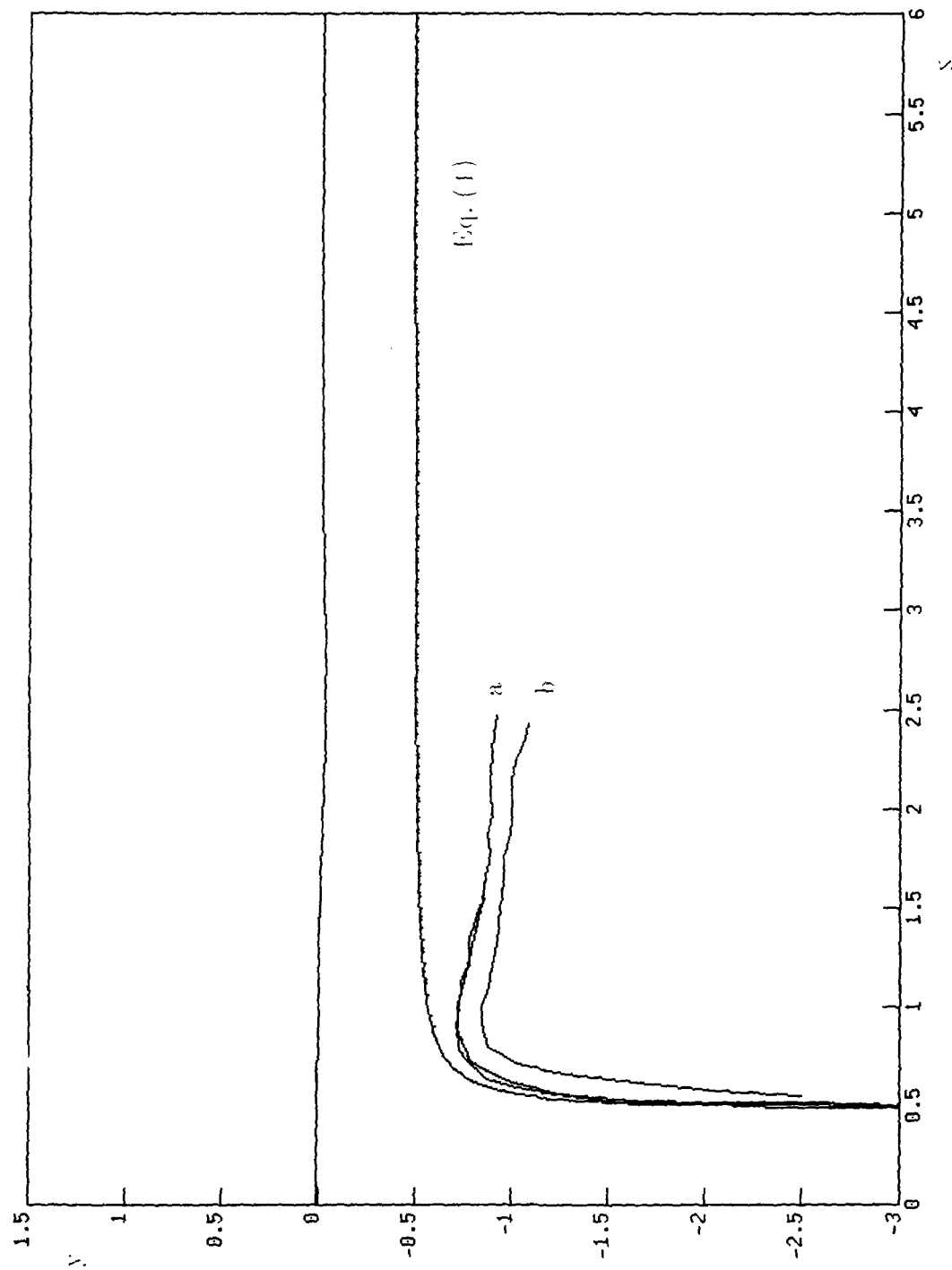**Fig. 32.** Free-surface vorticity for $Re = 50$, $Fr = 0.356$ at (a) $t = 3.52$, (b) $t = 5.02$, and (c) $t = 6.52$.

Fig. 33. Path of the vortex center for $Re = 50$, $Fr = 0.356$, defined (a) by $|\omega_{min}|$ for both fine and coarse grids, (b) by the center of the whirl. For comparison, Lamb's solution, Eq. (1), is added. The two curves (a) are almost indistinguishable.
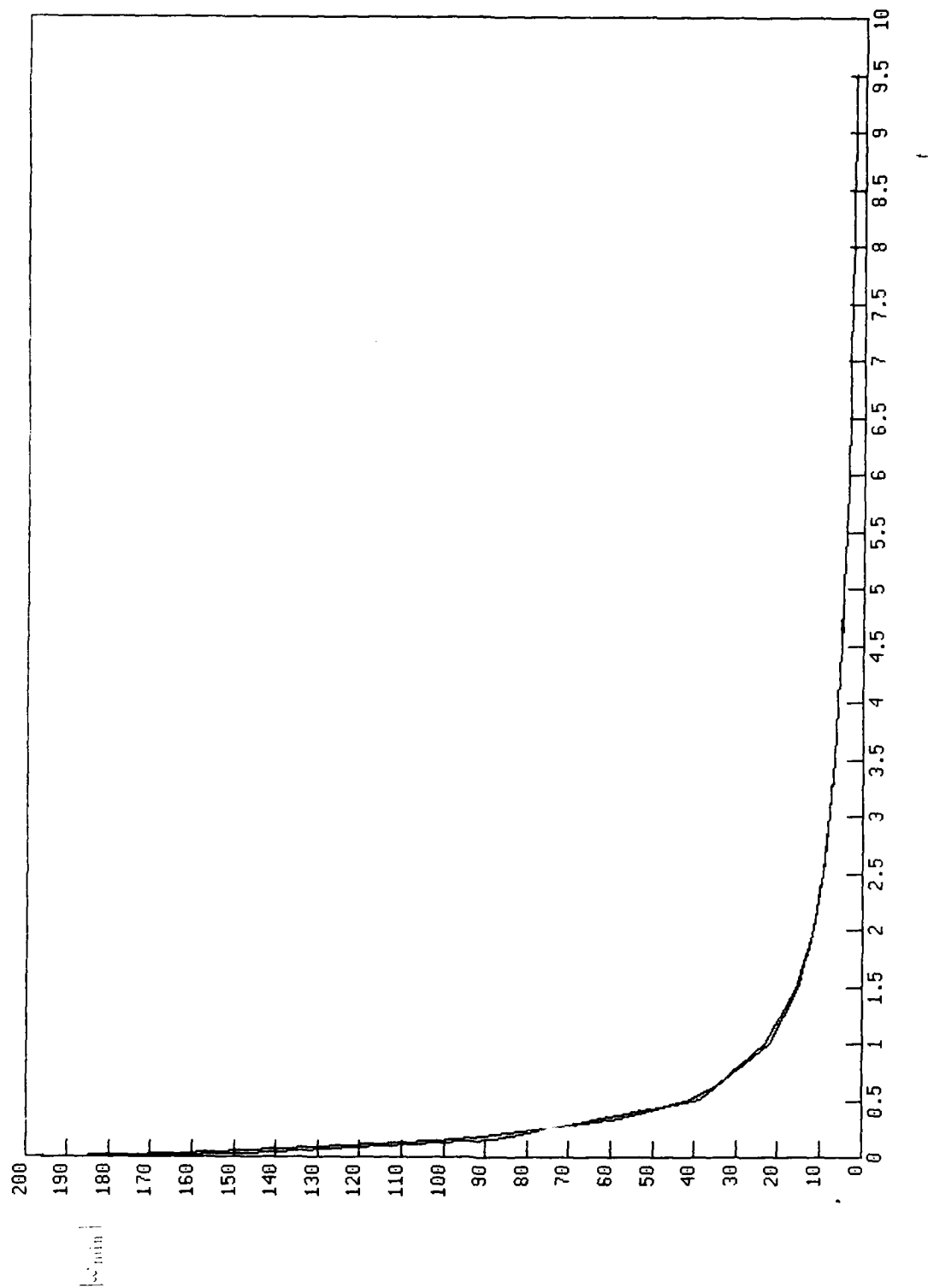
54

Fig. 34. Decrease of $|\dot{z}_{\min}|$ with time for $Re = 50$, $Pr = 0.356$ for both fine and coarse grids. The two curves are almost indistinguishable.

INITIAL DISTRIBUTION

Copies

1 DARPA

4 ONR
   1 R. Whitehead
   1 J. Fein
   1 E.P. Rood
   1 M. Reischmann

3 NAVSEA
   1 SEA 05, RADM Ricketts
   1 W. Sandberg
   1 Lib

2 USNA
   1 R.A. Granger
   1 Tech Lib

5 NRL
   1 Library
   1 O.M. Griffin
   1 R. Leighton
   1 M. Stewart
   1 H.T. Wang

2 NAVPGSCOL
   1 Lib
   1 T. Sarpkaya

1 NSWC/Dahlgren/Lib

1 NSWC/Whiteoak/Lib

1 Naval Ship Eng Cent Tech Lib

12 DTIC

1 Library of Congress
   1 Science and Tech Division

1 NASA Langley Res Center/Lib

2 NASA Ames Res Center
   1 Library
   1 B.G. McLachlan

1 NASA Lewis Res Center/Lib

1 Air Force Flight Dynamics Lab/Lib

1 U.S. Army Ballistic Res Lab/Lib

1 NIST/Lib

4 Univ of California, Berkeley
   1 Library
   1 S.A. Berger
   1 J.V. Wehausen
   1 R.W. Yeung

2 Univ of California, San Diego
   1 Library
   1 M. Gharib

2 Calif Inst of Tech
   1 Library
   1 T.Y. Wu

2 Univ of Iowa
   1 Library
   1 V.C. Patel

2 Lawrence Livermore Nat Lab
   1 Library
   1 D.L. Marcus

2 Univ of Maryland
   1 Library
   1 C. von Kerczek

6 Univ of Michigan
   1 Library
   1 R.F. Beck
   1 L. Bernal
   1 A.W. Troesch
   1 G. Tryggvason
   1 W.W. Willmarth

4 MIT
   1 Library
   1 J.N. Newman
   1 T.F. Ogilvie
   1 G.S. Triantafyllou

CENTER DISTRIBUTION (Continued)

Copies	Code	Name
1	00	C. Graham
1	01	R. Metrey
1	01A	D.D. Moran
1	01B	D.J. Clark
1	011	E. O'Neill
5	0113	B.E. Douglas
1	0117	B. Nakonechny
1	15	W.B. Morgan
1	1501	W.-C. Lin
1	1501	H.J. Haussling
1	1501	R.M. Coleman
1	154	J.H. McCarthy
1	1542	T.T. Huang
1	1543	L.P. Purtell
1	1544	F.B. Peterson
1	1544	A.M. Reed
1	156	D.S. Cieslowski
1	16	H.R. Chaplin
1	18	C.M. Schoman
20	1802	H.J. Lugt
1	184	J.W. Schot
1	1843	R.T. Van Eseltine
20	1843	S. Ohring
10	522.6	Reports Control
1	522.1	TIC (C)
1	522.2	TIC (A)